Article

The ABC exporter IrtAB imports and reduces mycobacterial siderophores

https://doi.org/10.1038/s41586-020-2136-9

Received: 30 October 2019

Accepted: 24 February 2020

Published online: 25 March 2020

Check for updates

Fabian M. Arnold[1,6], Miriam S. Weber[2,6], Imre Gonda[1,6], Marc J. Gallenito[3], Sophia Adenau[1], Pascal Egloff[1,5], Iwan Zimmermann[1,5], Cedric A. J. Hutter[1], Lea M. Hürlimann[1], Eike E. Peters[4], Jörn Piel[4], Gabriele Meloni[3], Ohad Medalia[2] & Markus A. Seeger[1]✉

Intracellular replication of the deadly pathogen *Mycobacterium tuberculosis* relies on the production of small organic molecules called siderophores that scavenge iron from host proteins[1]. *M. tuberculosis* produces two classes of siderophore, lipid-bound mycobactin and water-soluble carboxymycobactin[2,3]. Functional studies have revealed that iron-loaded carboxymycobactin is imported into the cytoplasm by the ATP binding cassette (ABC) transporter IrtAB[4], which features an additional cytoplasmic siderophore interaction domain[5]. However, the predicted ABC exporter fold of IrtAB is seemingly contradictory to its import function. Here we show that membrane-reconstituted IrtAB is sufficient to import mycobactins, which are then reduced by the siderophore interaction domain to facilitate iron release. Structure determination by X-ray crystallography and cryo-electron microscopy not only confirms that IrtAB has an ABC exporter fold, but also reveals structural peculiarities at the transmembrane region of IrtAB that result in a partially collapsed inward-facing substrate-binding cavity. The siderophore interaction domain is positioned in close proximity to the inner membrane leaflet, enabling the reduction of membrane-inserted mycobactin. Enzymatic ATPase activity and in vivo growth assays show that IrtAB has a preference for mycobactin over carboxymycobactin as its substrate. Our study provides insights into an unusual ABC exporter that evolved as highly specialized siderophore-import machinery in mycobacteria.

After biosynthesis, mycobactins are exported from the cytoplasm by the inner-membrane RND transporters MmpL4 and MmpL5, a process that also requires the periplasmic adaptor proteins MmpS4 and MmpS5[6]. At the level of the outer membrane, the EXS-3 secretion system is needed for mycobactin-mediated iron acquisition[7], which probably involves secreted effector proteins[8]. Finally, the heterodimeric ABC transporter IrtAB—which comprises the proteins IrtA and IrtB—imports iron-bound carboxymycobactin (cMBT) across the inner membrane, and its deletion attenuates the replication of *M. tuberculosis* in mice[4]. ABC transporters constitute a large family of membrane transporters, which couple the binding and hydrolysis of ATP at a pair of highly conserved nucleotide-binding domains (NBDs) to conformational changes in variable transmembrane domains (TMDs)[9]. However, the import function of IrtAB is contradictory to structural predictions, which suggest that it has an ABC exporter fold. As the name suggests, ABC exporters are typically involved in the export of substrates out of the cell; canonical ABC importers feature TMDs that are very distinct from those of ABC exporters and depend on additional substrate-binding domains in order to accomplish substrate uptake[9,10]. An additional unusual feature of IrtAB is a siderophore interaction domain (SID) fused to the N terminus of IrtA—this has been suggested, although not shown in vitro, to reduce Fe(III)-cMBT in order to facilitate the release of iron inside the bacterial cell[5].

To gain structural insights into this unusual ABC exporter, we used X-ray crystallography and single particle cryo-electron microscopy (cryo-EM) to determine the structure of the IrtAB protein of *Mycobacterium thermoresistibile*. IrtAB of this thermophilic mycobacterial species was found to be amenable to structural and biochemical analyses. Notably, IrtAB of *M. thermoresistibile* shares 71% sequence identity with the *M. tuberculosis* homologue (Extended Data Fig. 1a). A cryo-EM structure of full-length IrtAB was obtained at a global resolution of 6.9 Å, and features an unambiguous density for the transporter as well as for the SID (Fig. 1a, Extended Data Figs. 2, 3, Extended Data Table 1). With the aid of a synthetic nanobody (sybody)[11] that was identified using flycode technology[12], the crystal structure of IrtAB lacking the SID was solved at a resolution of 2.7 Å in its apo state (Extended Data Fig. 1b, Extended Data Table 2). The transporter assumes an inward-facing conformation in which the NBDs contact each other via a C-terminal extension of the NBD of IrtB. A search of the DALI server for similar protein folds clearly marked IrtAB as an ABC exporter[13]. With a root-mean-square deviation (r.m.s.d.) of 5.9 Å over the entirety of the polypeptide chains, the heterodimeric IrtAB complex features major asymmetries[14], which enabled us to unambiguously assign the identity of the chains within the cryo-EM map (Fig. 1a). Superimpositions of the structure with those of other ABC exporters showed that IrtAB had the highest similarity

[1]Institute of Medical Microbiology, University of Zurich, Zurich, Switzerland. [2]Department of Biochemistry, University of Zurich, Zurich, Switzerland. [3]Department of Chemistry and Biochemistry, University of Texas at Dallas, Richardson, TX, USA. [4]Institute of Microbiology, ETH Zurich, Zurich, Switzerland. [5]Present address: Linkster Therapeutics, Zurich, Switzerland. [6]These authors contributed equally: Fabian M. Arnold, Miriam S. Weber, Imre Gonda. ✉e-mail: m.seeger@imm.uzh.ch

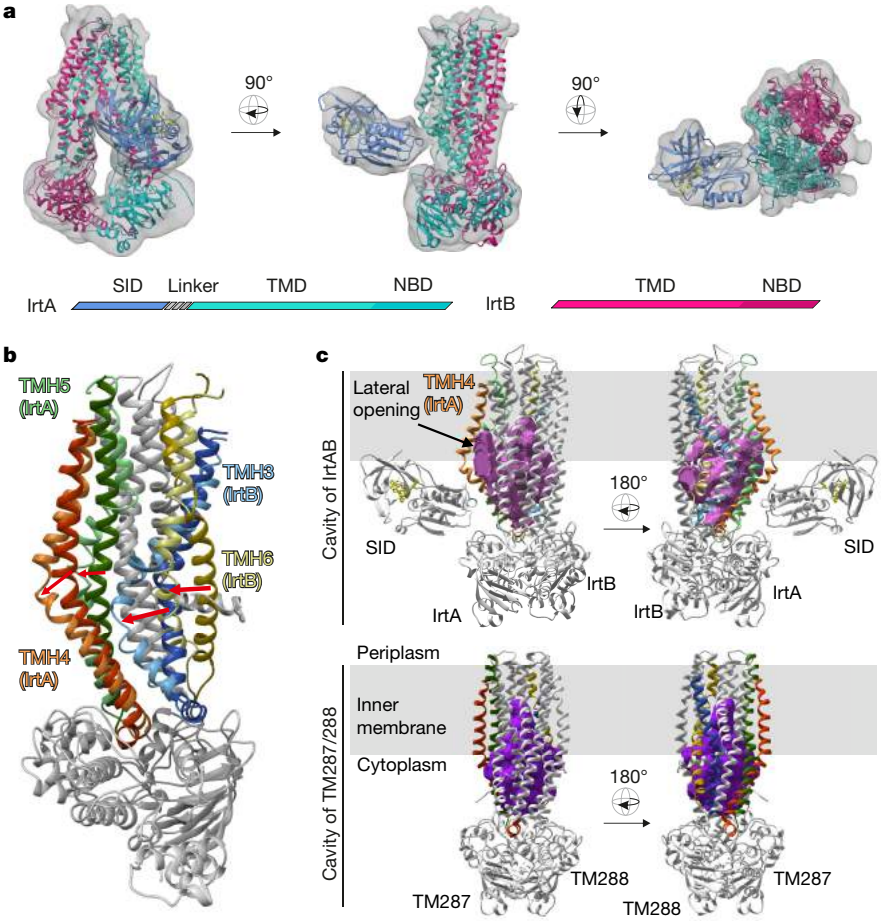

Fig. 1 | Structure of IrtAB. a, X-ray structures of IrtAB lacking the SID (2.7 Å resolution; IrtA in turquoise and IrtB in magenta) and of the isolated SID (1.8 Å resolution; the SID is shown in blue with the bound FAD molecule shown in yellow as sticks) were fitted into the cryo-EM map (6.9 Å resolution) of full-length IrtAB. The domain organization of the IrtAB heterodimer is shown at the bottom. **b**, Superimposition of IrtB plus domain-swap-helices TMH4 and TMH5 of IrtA with TM288 plus domain-swap-helices TMH4 and TMH5 of TM287. TMH6 (IrtB, TM288), TMH3 (IrtB, TM288), TMH4 (IrtA, TM287) and TMH5 (IrtA, TM287) are coloured as indicated and the rest is shown in grey. Arrows indicate the structural changes from TM287/288 (darker colours) to IrtAB (lighter colours). **c**, Inward-facing cavities of IrtAB and TM287/288 (PDB: 4Q4A). TMHs with strong differences between IrtAB and TM287/288 are coloured as in **b**. The inward-facing cavity of IrtAB is collapsed at the upper third compared to TM287/288, mainly due to the movement of TMH6 of IrtB. The bulged-out domain swap helices TMH4 and TMH5 of IrtA result in a lateral access to the cavity from the inner leaflet of the lipid bilayer (indicated in grey).

to the inward-facing structure of TM287/288 (ref. [15]) (Extended Data Fig. 4), and further revealed three conspicuous structural peculiarities of IrtAB: first, transmembrane helix 6 (TMH6) of IrtB protrudes into the central cavity; second, TMH3 of IrtB threads underneath TMH6 and is strongly kinked; and third, the domain-swap helices (TMH4 and TMH5) of IrtA are bulged out (Fig. 1b). As a result, the inward-facing cavity of IrtAB is collapsed at the upper region. Further, the bulged-out domain swap helices form a lateral opening from the cavity to the inner leaflet of the lipid bilayer at the side of the transporter, where the SID is located (Fig. 1c). Therefore, in contrast to canonical ABC exporters—in which the inward-facing conformation represents the high-affinity state that enables substrate binding to a deep cavity—the inward-facing conformation of IrtAB may represent the low-affinity state after mycobactin release towards the SID and the cytoplasm.

The X-ray structure of the SID was determined at 1.8 Å resolution (Fig. 2c, Extended Data Table 2). It exhibits a conserved flavoreductase fold and features an electron-donor pocket, a perpendicularly located substrate pocket and a flavin adenine dinucleotide (FAD) molecule bound between the pockets[16]. The SID could be unambiguously placed into the cryo-EM map, and is positioned close to the predicted membrane boundary through protein interactions with the TMD of IrtA (Fig. 1a). The 72-amino-acid linker between the SID and the first 'elbow' helix of the TMD of IrtA is not visible in the map, presumably because of its flexibility. Notably, the presumed mycobactin-binding pocket of the SID is positioned such that it can accommodate Fe-MBT embedded in the cytoplasmic leaflet of the inner membrane, which suggests that the SID has an important role in iron scavenging via Fe-MBT (Extended Data Fig. 5).

In many ABC transporters, the ATPase activity is stimulated by the presence of transported substrates[17–19]. To measure ATPase activities in a lipid environment, purified wild-type IrtAB from *M. thermoresistibile* was reconstituted into nanodiscs. In analogy to previous studies of the ABC transporter P-glycoprotein[20], we mutated the catalytic Walker B glutamates of both nucleotide-binding sites to glutamine (IrtA(E815Q)–IrtB(E493Q), henceforth denoted the 2×EQ mutant), and used this mutant protein as the ATPase-deficient control throughout the study. The ATPase activity of reconstituted wild-type IrtAB was stimulated more than 38-fold in the presence of Fe-MBT, and more than 10-fold in the presence of Fe-cMBT (Fig. 2a). For Fe-cMBT, but not for Fe-MBT, the ATPase activity decreases again at concentrations greater than 10 μM. Bell-shaped drug-stimulation curves such as this are frequently observed for ABC transporters and arise when the substrate occupies a secondary, low-affinity binding site, thus slowing the ATPase cycle[17,21]. In contrast to mycobactins, ethidium and Hoechst 33342—two

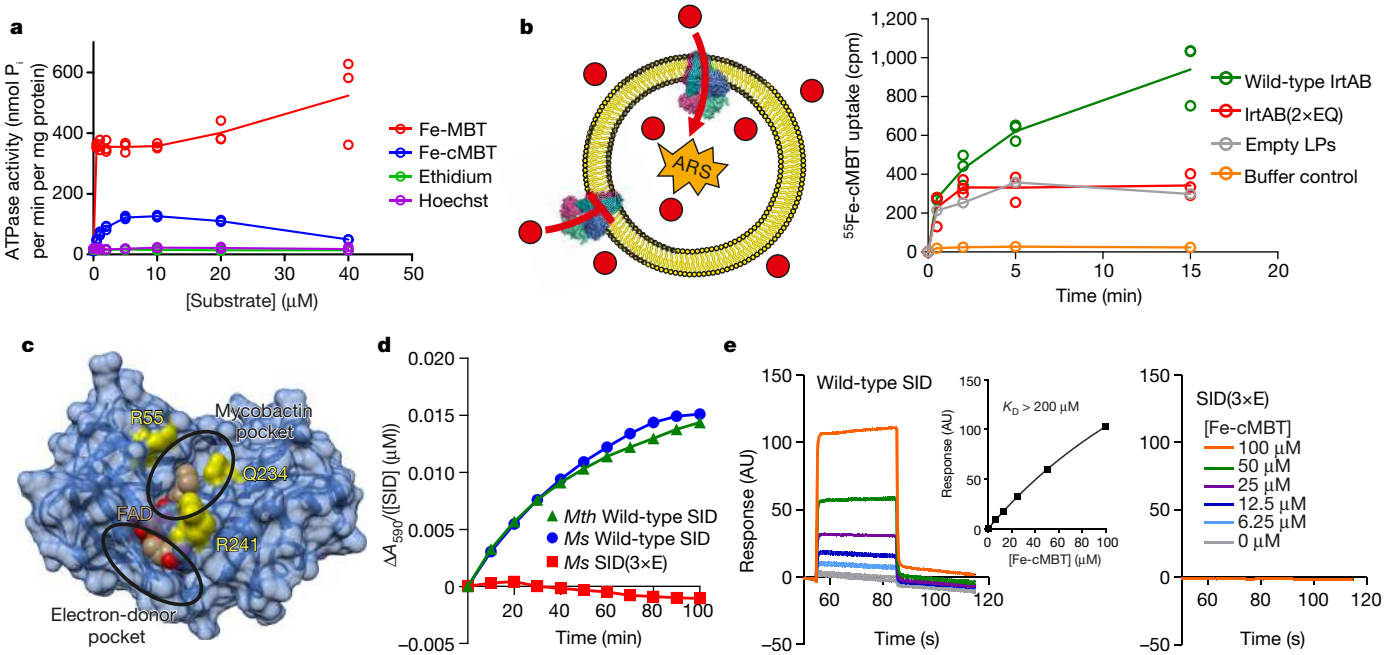

Fig. 2 | Biochemical characterization of IrtAB. a, ATPase activity of IrtAB reconstituted into nanodiscs in the presence of increasing concentrations of Fe-MBT, Fe-cMBT, ethidium and Hoechst. Data points are technical triplicates and curves cross through the mean values. **b**, In vitro transport of Fe-cMBT mediated by wild-type IrtAB and inactive IrtAB(2×EQ) reconstituted into proteoliposomes. Left, an ATP-regenerating system (ARS) was incorporated into the vesicle lumen. Right, uptake of radiolabelled ^{55}Fe-cMBT into the vesicle lumen was measured over time. As a control, the assay was performed with empty liposomes (LPs) or buffer only. For the wild-type and the 2×EQ mutant, data points are technical triplicates and the curves cross through the mean values. **c**, Structure of the SID with the electron-donor pocket and the mycobactin pocket highlighted. FAD is shown as spheres and coloured in beige. To generate the 3×E mutant, three conserved residues lining the mycobactin pocket (yellow) were mutated to glutamate. **d**, Reduction of Fe(III)-cMBT by the SIDs of *M. thermoresistibile* (*Mth*) and *M. smegmatis* (*Ms*) using NADPH as electron donor and ferene as a reporter probe of released Fe(II) (A_{590}, absorbance at 590 nm). The mutant SID(3×E) served as negative control. Representative data of biological duplicates are shown. **e**, Binding of Fe-cMBT to the SID of *M. smegmatis* as measured by SPR. The concentrations are as indicated in the right panel. SPR sensorgrams were recorded for the wild-type SID (left) or the 3×E mutant (right). Fitting of equilibrium binding values indicated a K_D of greater than 200 μM (left, inset). The SPR experiment was performed once.

benchmark substrates of multidrug ABC exporters[17]—did not stimulate the ATPase activity of IrtAB. Experiments with HPLC-purified mycobactins revealed that the aliphatic chain length of cMBT or MBT does not have an influence on the ATPase stimulation of IrtAB (Extended Data Fig. 6).

Next, we investigated whether the ABC exporter IrtAB is sufficient for mycobactin import. To this end, purified *M. thermoresistibile* IrtAB—either wild-type or the inactive 2×EQ mutant—was reconstituted into liposomes[22]. This procedure results in the incorporation of membrane transporters in mixed orientations—that is, the ATP-consuming NBDs are either located in the lumen of the liposome or point to the bulk buffer (Fig. 2b). Directionality of transport was imposed by encapsulating an ATP-regeneration system inside the liposomes. The hydrophobic properties of Fe-MBT prevented us from performing transport assays with liposomes, and therefore in vitro transport assays were carried out with Fe-cMBT only. Transport experiments were initiated by adding radioactively labelled ^{55}Fe-cMBT to proteoliposomes, which were then separated from free ^{55}Fe-cMBT by rapid size-exclusion chromatography. Liposomes containing wild-type IrtAB showed greater uptake of ^{55}Fe-cMBT than those containing the inactive 2×EQ mutant (Fig. 2b). When empty liposomes were included as a control, the trace was very similar to that of liposomes containing the 2×EQ mutant, which indicates the unspecific interaction of ^{55}Fe-cMBT with the liposome membrane. When the assay was conducted with ^{55}Fe-cMBT in the absence of liposomes, the counts were very low, showing minimal leakage during the rapid size-exclusion chromatography step. Taken together, these results show that purified and reconstituted IrtAB is capable of ^{55}Fe-cMBT uptake in an ATPase-dependent manner.

To assess whether the SID is capable of reducing Fe(III)-cMBT to liberate Fe(II), as suggested by in vivo assays[5], we performed redox experiments with the SIDs from *Mycobacterium smegmatis* and *M. thermoresistibile* under strictly anaerobic conditions. We found that both Fe(III)-cMBT and Fe(III)-MBT were reduced in the presence of the SIDs using NADPH as electron donor (Fig. 2d, Extended Data Fig. 7a). As a control, three conserved residues that line the presumed mycobactin-binding pocket (R55, Q234 and R241) of the SID of *M. smegmatis* were mutated to glutamate (denoted the 3×E mutant) (Fig. 2c). The purified 3×E mutant eluted as a monomeric peak from a size-exclusion chromatography column without any indication of misfolding, but was no longer capable of reducing Fe(III)-cMBT and Fe(III)-MBT (Fig. 2d, Extended Data Fig. 7a). We noted that the estimated catalytic rates of the wild-type SID were at least an order of magnitude lower than those previously published for siderophore-interacting proteins[16]. By measuring reduction rates at different concentrations of Fe(III)-MBT, we determined that the SID of *M. thermoresistibile* had an apparent Michaelis constant (K_M) for mycobactin of 185 μM (Extended Data Fig. 7b). This was confirmed in a surface plasmon resonance binding (SPR) experiment, which suggested that the dissociation constant (K_D) for Fe-cMBT with the SID of *M. smegmatis* is greater than 200 μM (Fig. 2e). Measurement artefacts in the SPR experiment could be excluded, because Fe-cMBT was not observed to bind to the SID 3×E mutant.

To analyse mycobactin-mediated iron acquisition through IrtAB, we generated the double-mutant *M. smegmatis* Δ*fxbA*Δ*mbtD*, hereafter denoted DKO. In this mutant, the deletion of the *fxbA* and *mbtD* genes abrogate the biosynthesis of exochelin—an additional siderophore produced by *M. smegmatis*—and mycobactin, respectively[23].

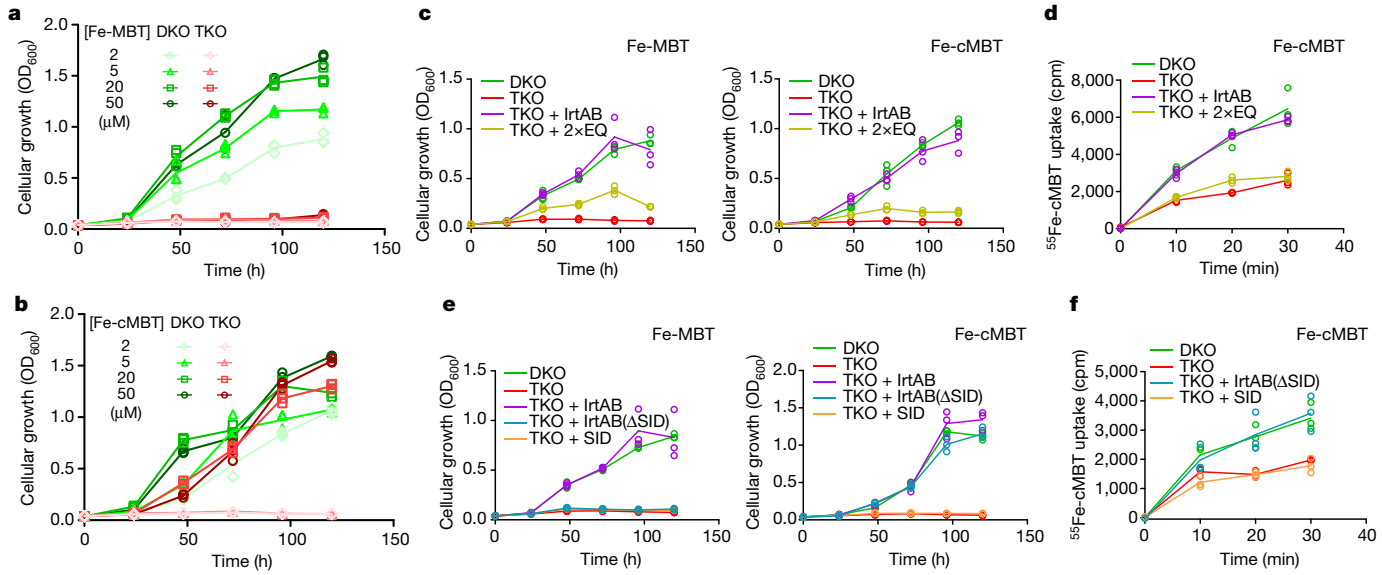

Fig. 3 | In vivo characterization of IrtAB in *M. smegmatis*. **a**, **b**, Mycobactin-dependent growth of the DKO and TKO *M. smegmatis* mutants in the presence of Fe-MBT (**a**) or Fe-cMBT (**b**) added at the indicated concentrations. **c**–**f**, Complementation of the TKO strain with full-length IrtAB (wild-type), the IrtAB mutant devoid of ATPase activity (2×EQ), IrtAB devoid of the SID (IrtAB(ΔSID)) and the SID alone (SID). **c**, **e**, Mycobactin-dependent growth determined in the presence of 2 μM Fe-MBT (left) or 2 μM Fe-cMBT (right). **d**, **f**, Cellular uptake of radiolabelled ^{55}Fe-cMBT. Data points are technical triplicates and curves cross through the mean values.

Subsequently, we generated the triple-mutant *M. smegmatis* Δ*fxbA*Δ*mbtD*Δ*irtAB* (hereafter TKO), which also lacks IrtAB. Wild-type, DKO and TKO *M. smegmatis* were grown in minimal medium in the presence of the weak iron chelator 2,2′-dipyridyl to achieve conditions in which siderophores become essential for growth[7,23]. As expected, wild-type cells were able to grow under these conditions owing to their capacity to produce siderophores, whereas no growth was observed for DKO and TKO cells (Extended Data Fig. 8). When purified Fe-MBT was added to the medium as an iron source at concentrations ranging from 2 μM to 50 μM, DKO cells grew whereas TKO cells—lacking the IrtAB transporter—did not (Fig. 3a). However, when Fe-cMBT was added at 20 μM or 50 μM, the growth of both DKO and TKO cells was rescued; this suggests the presence of an alternative import protein for Fe-cMBT in addition to IrtAB (Fig. 3b). The TKO strain stopped growing only at Fe-cMBT concentrations of 2 μM or 5 μM (Fig. 3b). Hence, IrtAB acts as high-affinity importer for Fe-cMBT. In agreement with this, we found that the ATPase of IrtAB was maximally stimulated at an Fe-cMBT concentration of around 5 μM (Fig. 2a). Furthermore, for both Fe-cMBT and Fe-MBT, low micromolar concentrations were sufficient to achieve maximal catalytic activity of the transporter in the ATPase-stimulation experiments. To ensure the best possible discrimination between the DKO and TKO strains, we added Fe-cMBT and Fe-MBT at 2 μM for subsequent in vivo growth assays.

To further investigate the function of IrtAB, the TKO strain was complemented with different *M. smegmatis* IrtAB constructs using the integrative pFlag vector[24]. The DKO strain was used as a positive control for growth, whereas TKO was used as a negative control. To assess whether ATP hydrolysis is required for transport, we complemented the TKO strain with IrtAB(2×EQ)—which is devoid of ATPase activity—and wild-type IrtAB. For both Fe-MBT and Fe-cMBT, complementation with wild-type IrtAB restored growth to the levels of the DKO strain (Fig. 3c). IrtAB(2×EQ) partially restored growth, suggesting that it either exhibits residual ATPase activity—as is the case for other ABC transporters[20]—or that IrtAB can act as a facilitator for mycobactins (Fig. 3c). To gain insights into shorter timescales of mycobactin uptake, we measured the cellular accumulation of ^{55}Fe-cMBT. The TKO strain showed slower ^{55}Fe-cMBT uptake than the DKO strain, and only expression of the wild-type transporter—but not the 2×EQ mutant—could complement ^{55}Fe-cMBT uptake in the TKO strain (Fig. 3d). Efficient uptake of mycobactins is therefore dependent on ATP hydrolysis. To investigate the role of the SID, we complemented the TKO strain with wild-type IrtAB, the isolated SID and the IrtAB transporter without SID (IrtAB(ΔSID)). Expression of the isolated SID did not restore growth when adding Fe-MBT or Fe-cMBT as the iron source (Fig. 3e). By contrast, the IrtAB(ΔSID) construct restored growth with Fe-cMBT but not with Fe-MBT, which suggests that cooperative transport and local reduction are required in order to utilize iron via Fe-MBT. We again measured cellular ^{55}Fe-cMBT uptake at shorter timescales, which confirmed our finding that IrtAB(ΔSID) efficiently imports Fe-cMBT (Fig. 3f).

Previous studies have suggested that IrtAB is primarily responsible for the import of Fe-cMBT[4]. On the basis of our experiments, we show here that Fe-MBT is preferred over Fe-cMBT as a substrate for IrtAB. First, the ATPase activity of purified and reconstituted IrtAB is stimulated much more strongly in the presence of Fe-MBT compared with Fe-cMBT, and reaches its maximum at Fe-MBT concentrations as low as 0.5 μM (Fig. 2a). Second, IrtAB is essential for the uptake and utilization of Fe-MBT as an iron source over a broad range of concentrations, whereas it is dispensable for growth at increased Fe-cMBT concentrations—most likely due to the presence of an alternative Fe-cMBT import system in addition to IrtAB (Fig. 3a, b). Third, the SID of IrtAB is required for growth when using Fe-MBT as an iron source, but not when iron is supplied through Fe-cMBT (Fig. 3e). The uptake of externally added Fe-cMBT and Fe-MBT appears to function similarly well, because both forms of mycobactin support cellular growth under otherwise iron-depleted conditions in a similar concentration range (Fig. 3a, b). Our findings are in agreement with a previous study showing that both forms of mycobactin are secreted by mycobacteria—namely into the aqueous surroundings in the case of cMBT and embedded into secreted membrane vesicles in the case of MBT[25]. By this means, *M. tuberculosis* can access different iron stores present in the infected cell.

Our experiments unambiguously demonstrate that IrtAB is a mycobactin importer; however, IrtAB clearly has the fold of an ABC exporter. To our knowledge, ABC exporters that import substrates have so far been described only for the human *N*-retinylidene-phosphatidylethanolamine transporter ABCA4, the cobalamin transporter ABCD4 and the plant auxin ABC transporter AtPGP4[26–28]. Our in vitro transport

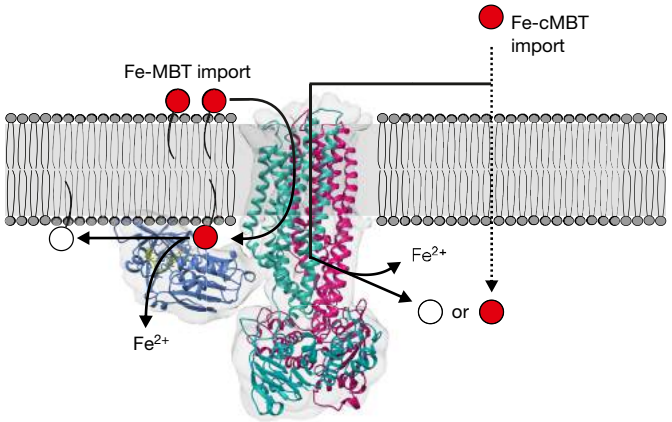

Fig. 4 | Proposed mechanism of IrtAB-mediated mycobactin uptake. IrtAB imports both Fe-MBT and Fe-cMBT across the inner membrane. For Fe-cMBT, an alternative import mechanism exists. After import, Fe-MBT remains anchored to the membrane and is thereby ideally positioned for reduction by the SID. The SID is essential for iron utilization via Fe-MBT, but not via Fe-cMBT. Iron-bound mycobactins are shown in red, desferrated mycobactins are shown in white.

experiments clearly demonstrate that IrtAB does not depend on additional proteins in order to accomplish ferric mycobactin import. Therefore, the transport mechanism must be distinct from that of classical ABC importers, the function of which depend on periplasmic-binding proteins.

In conclusion, IrtAB imports membrane bound Fe-MBT from the periplasmic to the cytoplasmic leaflet of the inner mycobacterial membrane (Fig. 4). Upon import by IrtAB, the local concentration of Fe-MBT in proximity to the transporter is expected to be higher than that of Fe-cMBT, because Fe-MBT remains confined to the inner membrane. In this context, the SID is ideally positioned for the reduction of Fe-MBT, which explains why the SID is essential for iron uptake via Fe-MBT. This high local concentration probably compensates for the low binding affinities and slow catalytic rates of the SID that are measured in vitro. By contrast, the SID is dispensable for iron utilization via Fe-cMBT, because this soluble form of mycobactin can freely diffuse into the cytoplasm after import where it may be reduced by other ferric reductases. It is highly likely that IrtAB specifically recognizes the iron-binding core that is common to Fe-MBT and Fe-cMBT via amino acid side chains within the TMDs, which will require identification in future studies. It is further conceivable that the lipid tail of Fe-MBT remains embedded in the lipid bilayer during the import reaction, in analogy to the 'credit-card-swipe mechanism' that has been described for the glycolipid ABC transporter PglK[29]. Our findings open avenues to study the transport mechanism of this unusual ABC exporter in more detail, whereas its structural elucidation provides a basis from which to exploit IrtAB as a potential drug target to develop novel antibiotics against *M. tuberculosis*.

Online content

Any methods, additional references, Nature Research reporting summaries, source data, extended data, supplementary information, acknowledgements, peer review information; details of author contributions and competing interests; and statements of data and code availability are available at https://doi.org/10.1038/s41586-020-2136-9.

1. De Voss, J. J. et al. The salicylate-derived mycobactin siderophores of *Mycobacterium tuberculosis* are essential for growth in macrophages. *Proc. Natl Acad. Sci. USA* **97**, 1252–1257 (2000).
2. Snow, G. A. & White, A. J. Chemical and biological properties of mycobactins isolated from various mycobacteria. *Biochem. J.* **115**, 1031–1045 (1969).
3. Gobin, J. et al. Iron acquisition by *Mycobacterium tuberculosis*: isolation and characterization of a family of iron-binding exochelins. *Proc. Natl Acad. Sci. USA* **92**, 5189–5193 (1995).
4. Rodriguez, G. M. & Smith, I. Identification of an ABC transporter required for iron acquisition and virulence in *Mycobacterium tuberculosis*. *J. Bacteriol.* **188**, 424–430 (2006).
5. Ryndak, M. B., Wang, S., Smith, I. & Rodriguez, G. M. The *Mycobacterium tuberculosis* high-affinity iron importer, IrtA, contains an FAD-binding domain. *J. Bacteriol.* **192**, 861–869 (2010).
6. Wells, R. M. et al. Discovery of a siderophore export system essential for virulence of *Mycobacterium tuberculosis*. *PLoS Pathog.* **9**, e1003120 (2013).
7. Siegrist, M. S. et al. Mycobacterial Esx-3 is required for mycobactin-mediated iron acquisition. *Proc. Natl Acad. Sci. USA* **106**, 18792–18797 (2009).
8. Tufariello, J. M. et al. Separable roles for *Mycobacterium tuberculosis* ESX-3 effectors in iron acquisition and virulence. *Proc. Natl Acad. Sci. USA* **113**, E348–E357 (2016).
9. Locher, K. P. Mechanistic diversity in ATP-binding cassette (ABC) transporters. *Nat. Struct. Mol. Biol.* **23**, 487–493 (2016).
10. ter Beek, J., Guskov, A. & Slotboom, D. J. Structural diversity of ABC transporters. *J. Gen. Physiol.* **143**, 419–435 (2014).
11. Zimmermann, I. et al. Synthetic single domain antibodies for the conformational trapping of membrane proteins. *eLife* **7**, e34317 (2018).
12. Egloff, P. et al. Engineered peptide barcodes for in-depth analyses of binding protein libraries. *Nat. Methods* **16**, 421–428 (2019).
13. Holm, L. & Laakso, L. M. Dali server update. *Nucleic Acids Res.* **44**, W351–W355 (2016).
14. Hutter, C. A. J. et al. The extracellular gate shapes the energy profile of an ABC exporter. *Nat. Commun.* **10**, 2260 (2019).
15. Hohl, M., Briand, C., Grütter, M. G. & Seeger, M. A. Crystal structure of a heterodimeric ABC transporter in its inward-facing conformation. *Nat. Struct. Mol. Biol.* **19**, 395–402 (2012).
16. Miethke, M., Hou, J. & Marahiel, M. A. The siderophore-interacting protein YqjH acts as a ferric reductase in different iron assimilation pathways of *Escherichia coli*. *Biochemistry* **50**, 10951–10964 (2011).
17. Hürlimann, L. M. et al. The heterodimeric ABC transporter EfrCD mediates multidrug efflux in *Enterococcus faecalis*. *Antimicrob. Agents Chemother.* **60**, 5400–5411 (2016).
18. Ambudkar, S. V. et al. Partial purification and reconstitution of the human multidrug-resistance pump: characterization of the drug-stimulatable ATP hydrolysis. *Proc. Natl Acad. Sci. USA* **89**, 8472–8476 (1992).
19. Lee, J. Y., Yang, J. G., Zhitnitsky, D., Lewinson, O. & Rees, D. C. Structural basis for heavy metal detoxification by an Atm1-type ABC exporter. *Science* **343**, 1133–1136 (2014).
20. Tombline, G., Bartholomew, L. A., Urbatsch, I. L. & Senior, A. E. Combined mutation of catalytic glutamate residues in the two nucleotide binding domains of P-glycoprotein generates a conformation that binds ATP and ADP tightly. *J. Biol. Chem.* **279**, 31212–31220 (2004).
21. Al-Shawi, M. K., Polar, M. K., Omote, H. & Figler, R. A. Transition state analysis of the coupling of drug transport to ATP hydrolysis by P-glycoprotein. *J. Biol. Chem.* **278**, 52629–52640 (2003).
22. Geertsma, E. R., Nik Mahmood, N. A., Schuurman-Wolters, G. K. & Poolman, B. Membrane reconstitution of ABC transporters and assays of translocator function. *Nat. Protoc.* **3**, 256–266 (2008).
23. Dragset, M. S. et al. Genome-wide phenotypic profiling identifies and categorizes genes required for mycobacterial low iron fitness. *Sci. Rep.* **9**, 11394 (2019).
24. Arnold, F. M. et al. A uniform cloning platform for mycobacterial genetics and protein production. *Sci. Rep.* **8**, 9539 (2018).
25. Prados-Rosales, R. et al. Role for *Mycobacterium tuberculosis* membrane vesicles in iron acquisition. *J. Bacteriol.* **196**, 1250–1256 (2014).
26. Quazi, F., Lenevich, S. & Molday, R. S. ABCA4 is an *N*-retinylidene-phosphatidylethanolamine and phosphatidylethanolamine importer. *Nat. Commun.* **3**, 925 (2012).
27. Xu, D. et al. Cryo-EM structure of human lysosomal cobalamin exporter ABCD4. *Cell Res.* **29**, 1039–1041 (2019).
28. Santelia, D. et al. MDR-like ABC transporter AtPGP4 is involved in auxin-mediated lateral root and root hair development. *FEBS Lett.* **579**, 5399–5406 (2005).
29. Perez, C. et al. Structure and mechanism of an active lipid-linked oligosaccharide flippase. *Nature* **524**, 433–438 (2015).

Methods

Data reporting

No statistical methods were used to predetermine sample size. The experiments were not randomized and the investigators were not blinded to allocation during experiments and outcome assessment.

Strains, media and antibiotic concentrations

Escherichia coli XL1-Blue was used for cloning of open reading frames (ORFs), complementation constructs and gene deletions. *E. coli* MC1061 strain was used for expression of ORFs in *E. coli*. Luria Broth (LB) was used for liquid cultures, and Luria Broth Agar (LB Agar) for plates. For protein expression, terrific broth (TB) was used for liquid cultures. Antibiotics were used in the following concentrations for *E. coli*: ampicillin 100 μg ml^{-1}, kanamycin 50 μg ml^{-1}, chloramphenicol 25 μg ml^{-1}, apramycin 50 μg ml^{-1} and hygromycin 100 μg ml^{-1}. The *M. smegmatis* mc^{2}155 strain was used for all in vivo experiments, for the generation of deletion mutants and the generation of complementation strains. When culturing the cells in iron-rich medium, 7H9 with OADC supplement was used for liquid cultures, and 7H10 with OADC supplement was used for plates. Antibiotics were used in the following concentrations for *M. smegmatis*: kanamycin 25 μg ml^{-1}, apramycin 25 μg ml^{-1} and hygromycin 50 μg ml^{-1}. When culturing the cells under low-iron conditions, minimal medium was prepared according to ref. [30]. One litre of minimal medium contained 5 g KH_2PO_4, 5 g L-asparagine and 60 ml glycerol. The pH was set to 7.0 and the medium was autoclaved with 2% (w/v) aluminium oxide. After autoclaving, the medium was filtered with a 0.22-μm filter (Whatman). The pH was set to 6.8 using HCl and autoclaved again. Before use, the medium was supplemented with 6.88 μM $ZnSO_4$, 1.82 μM $MnSO_4$ and 1.64 mM $MgSO_4$. Unless stated otherwise, cells were incubated and grown at 37 °C.

Siderophore production and isolation

For production of MBT, minimal medium in glass flasks was inoculated 1:1,000 with *M. smegmatis* mc^{2}155 grown to stationary phase in 7H9 medium. The cultures were grown by shaking until they reached stationary phase (typically 5 to 6 days). MBT extraction was performed according to ref. [2]. In brief, cells were centrifuged at 8,000*g* for 1 h at 4 °C, and then taken up in 100% ethanol in 1:10 of the culture volume. MBT extraction was performed overnight by stirring at room temperature. The extract was filtered through a filter paper (Whatman) and one volume of chloroform was added to generate a monophasic solution. Subsequently, 10% (w/v) $FeCl_3$ in 100% ethanol was added dropwise to the solution, until no further increase in red colour was observed. Water (75% of solvent volume) was added to form a biphasic solution (chloroform and water/ethanol phases). The chloroform phase containing MBT was washed twice with 1 volume of water, dried with anhydrous $MgSO_4$ and evaporated. The Fe-MBT crude extract was then taken up in 100% ethanol. For production of cMBT, minimal medium in plastic ware was inoculated 1:1,000 with a dense *M. smegmatis* Δ*fxBC* culture (grown in 7H9) and grown to stationary phase. Cells were then inoculated 1:100 into 100 ml minimal medium supplemented with 1.432 μM $(NH_4)_2Fe(II)(SO_4)_2{\cdot}6H_2O$ in 1-l plastic roller bottles (Corning) and grown to stationary phase by shaking. Extraction of cMBT was performed according to ref. [30]. In brief, cells were centrifuged at 8,000*g* for 1 h at 4 °C, and the supernatant filtered with a 0.22-μm filter (Whatman). The pH of the supernatant was set to 3.5 using HCl, and 10% (w/v) $FeCl_3$ in 100% ethanol was added dropwise until formation of precipitate was observed (ferric phosphate). The iron-saturated supernatant was then stirred for 1 h at room temperature. The mixture was centrifuged for 15 min at 8,000*g* at 4 °C, and the supernatant was extracted with 1 volume of ethyl acetate. The ethyl acetate phase containing Fe-cMBT was washed twice with 1 volume of H_2O, dried with $MgSO_4$ and evaporated. The Fe-cMBT crude extract was taken up in 100% ethanol.

Mass spectrometry analysis and HPLC purification of siderophores

Crude extracts of siderophores were analysed by electrospray ionization tandem mass spectrometry (ESI-MS/MS) with a Q-exactive spectrometer (Thermo Scientific). Single siderophore species were purified by HPLC using a Phenomenex Luna C18(2) reverse phase column. Fe-cMBT was eluted with a 20 to 80% acetonitrile gradient with a flow rate of 2 ml min^{-1}. Fe-MBT was eluted with a 20 to 100% acetonitrile gradient with a flow rate of 5 ml min^{-1}. The masses of the eluted species were confirmed with a Q-exactive spectrometer (Thermo Scientific). The solvent was evaporated and the single species were taken up in 100% ethanol for further experiments.

Cloning of ORFs

ORFs were amplified from genomic DNA and cloned into the pINIT vector and then into the respective expression vector according to the FX cloning protocol[31]. Full-length IrtAB of *M. thermoresistibile* was cloned using primers #1 and #2 (all primers are listed in Supplementary Table 1). The SID of *M. thermoresistibile* was cloned using primers #1 and #3. The truncated IrtAB construct lacking the SID and the linker between SID and TMD was cloned using primers #4 and #2. Full-length IrtAB of *M. smegmatis* (MSMEG 6553/6554) was cloned using primers #5 and #6. The SID of *M. smegmatis* was cloned using primers #5 and #7. The truncated IrtAB construct lacking the SID and the linker between SID and TMD (IrtAB(ΔSID)) was cloned using primers #8 and #6. The 2×EQ mutations (to form the mutant IrtA(E815Q)–IrtB(E493)) were introduced into *M. thermoresistibile* full-length IrtAB in two steps by QuikChange mutagenesis using primer pairs #9/#10 and #11/#12. The corresponding 2×EQ mutations (to form IrtA(E770Q)–IrtB(E493Q)) were introduced into *M. smegmatis* full-length IrtAB in two steps by QuikChange mutagenesis using primer pairs #13/#14 and #15/#16. The 3×E mutations (R55E/Q234E/R241E, to form SID(3×E)) were introduced into the *M. smegmatis* SID by QuikChange mutagenesis using primer pairs #17/#18 (R55E) and #19/#20 (Q234E and R241E). All ORFs and mutants cloned into the pINIT vector were completely sequenced. Using FX cloning, the SID constructs were subcloned into the *E. coli* expression vector pBXNH3 (Addgene, 47067). The *M. smegmatis* SID constructs (wild-type and 3×E mutant) were also subcloned into pBXNH3A (Addgene, 47075) for subsequent biotinylation via an Avi-tag. The *M. thermoresistibile* IrtAB constructs (full-length/ full-length 2×EQ and IrtAB(ΔSID)) were subcloned into the *E. coli* expression vector pBXC3GH (Addgene, 47070). For binder selection and SPR experiments the *M. thermoresistibile* IrtAB full-length construct was subcloned into the *E. coli* expression vector pBXCA3GH (Addgene, 47071). All *M. smegmatis* ORFs (full-length, full-length 2×EQ, IrtAB(ΔSID), SID) were subcloned into the mycobacterial complementation vector pFlag (Addgene, 110095).

Expression and purification of proteins in *E. coli*

Proteins were produced in and purified from *E. coli* MC1061 using TB medium containing 100 μg ml^{-1} ampicillin. Cells were grown for 2 h at 37 °C while shaking. The temperature was reduced to 25 °C and cells were induced after 1 h with 0.02% L-arabinose and grown overnight. To purify the SID proteins, cells were collected by centrifugation at 9,000*g* for 15 min at 4 °C. Cells were resuspended in TBS (20 mM Tris/HCl, 150 mM NaCl, pH 7.5) containing a spatula tip of DNase I. Cells were lysed with a Microfluidizer M-110P (Microfluidics) with three passes at 25 kPa. The lysate was first centrifuged for 30 min at 8,000*g* at 4 °C to remove cell debris. Imidazole was added to a final concentration of 20 mM to the supernatant, which was then loaded onto a Ni^{2+}-NTA gravity flow column (Qiagen). The column was washed with 20 column volumes of wash buffer (50 mM imidazole pH 7.5, 150 mM NaCl, 10% glycerol), and then eluted with 4 column volumes of elution buffer (200 mM imidazole pH 7.5, 150 mM NaCl, 10% glycerol). The elution

was concentrated to 2.5 ml with a 10-kDa cut-off concentrator (Merck Millipore) and desalted with a PD10 column (GE Healthcare). 3C protease was added and the sample was incubated overnight at 4 °C for cleavage of the His_{10}-tag. Cleaved samples were purified via reverse Ni^{2+}-NTA. Cleaved protein was eluted from the column with 4 volumes of TBS buffer. The samples were concentrated again and loaded onto a Superdex 200 Increase 10/300 GL (GE Healthcare) size-exclusion chromatography (SEC) column using TBS as running buffer. To purify the *M. thermoresistibile* IrtAB membrane protein constructs, cells were broken as described above, centrifuged at 8,000*g*, and membrane vesicles were collected by ultracentrifugation at 170,000*g* (all purification steps performed at 4 °C). Membrane vesicles were resuspended with TBS, flash-frozen and stored at −80 °C until further use. Resuspended membrane vesicles were extracted with 1% (w/v) *n*-dodecyl-β-D-maltopyranoside (β-DDM, Glycon Biochemicals) for 2 h, followed by ultracentrifugation at 170,000*g* for 30 min. Imidazole was added to a final concentration of 20 mM to the supernatant containing extracted membrane proteins, which was then loaded onto a Ni^{2+}-NTA gravity flow column. The purification was then performed as described for the SID constructs, with the following differences: first, 0.03% β-DDM was included in all buffers; second, concentrators with 100 kDa cut-off were used; third, after reverse-Ni^{2+}-NTA purification the sample was diluted 1:10 with ion exchange buffer (15 mM Tris/HCl pH 8.0, 20 mM NaCl, 0.03% β-DDM) and loaded onto a Resource-Q ion-exchange column (GE Healthcare). The protein was eluted over a NaCl gradient (10 mM–350 mM, main protein peak eluted at around 150 mM). The main peak was concentrated and separated by SEC using a Superose 6 Increase 10/300 GL (GE Healthcare) column and TBS containing different detergents as running buffer: 0.3% *n*-decyl-β-D-maltopyranoside (β-DM) for crystallization of IrtABΔSID; 0.015% β-DDM for samples used for cryo-EM; 0.03% β-DDM for subsequent reconstitution of full-length IrtAB into proteoliposomes.

Cryo-EM sample preparation and data acquisition

For structure determination by cryo-EM, 3 µl of detergent-purified *M. thermoresistibile* IrtAB at a concentration of 2.5 mg ml^{-1} was applied to glow-discharged holey carbon grids (Quantifoil, R 2/1 Cu 200 mesh, No. Q32288) and plunge-frozen in liquid ethane using a Vitrobot Mark IV (Thermo Fisher Scientific) operated at 100% humidity and 4 °C. Excess liquid was blotted before plunging for 6 s using a blot force of 1. The grids were imaged at 300 kV in a Titan Krios electron microscope (Thermo Fisher Scientific). Data were acquired in energy-filtering mode using a postcolumn quantum energy filter (Gatan) with a 20 eV slit and a K2 Summit direct electron detector (Gatan) operating in super-resolution mode. Data were recorded with SerialEM 3.5.8 in low-dose mode[32]. All micrographs were acquired at a nominal magnification of 45,455 with a pixel size of 1.1 Å (0.55 Å in super-resolution) at a defocus between −1.6 and −3.0 µm. Dose-fractionation was used with a frame exposure of 0.2 s at a total exposure time of 10 s (50 frames in total), corresponding to a total electron dose of approximately 85 e^{-} $Å^{-2}$.

Cryo-EM image processing

In total, 2,507 micrographs were recorded and processed with RELION 2.1 and RELION 3.0[33,34]. Frame-based motion correction and dose-weighting were performed with two-times downsampled movies using MotionCor2[35]. The contrast transfer function (CTF) was estimated using CTFFIND4[36]. Low-quality micrographs showing high defocus, high astigmatism or low resolution were excluded, resulting in 2,168 micrographs that were used for further processing steps. To generate a template for autopicking, 1,118 IrtAB particles were picked manually, extracted with a box size of 200 pixels and 2D classified into ten classes. These classes served as a reference for automated picking of 335,045 particles. Two rounds of 2D classification using a spherical mask of 160 Å were performed, reducing the number of particles to 167,781. These particles were used for 3D classification into 6 classes, using the mammalian P-glycoprotein (EMDB ID: 6007 (ref. [37])) at 40 Å as a starting reference. One class with 70,257 particles revealed distinct structural features of IrtAB with its SID and was subjected to auto-refinement. For 3D classification and the first 3D refinement, CTF-amplitude correction was performed only from the first CTF peak onwards. The refined structure was used to subtract the micelle from the raw particles, which were subjected to another round of 3D refinement, limiting the rotations to 1.5 degrees. The final unmasked map showed a resolution of 7.86 Å, based on the gold standard Fourier shell correlation (FSC) 0.143 criterion[33,38–40]. The structure was sharpened to 6.88 Å using an isotropic B-factor of −319 $Å^2$. The local resolution was estimated using BlocRes from the Bsoft package[41,42]. Directional Fourier shell correlation curves were calculated with the 3DFSC software[43].

Crystallization, data collection and structure determination of the *M. thermoresistibile* SID

M. thermoresistibile SID crystals were obtained in 400 mM ammonium acetate pH 8.0, 12% (v/v) PEG2000 at a protein concentration of 30 mg ml^{-1}. Crystals were frozen with 30% (v/v) ethylene glycol as cryo-protecting agent and measured at the Swiss Light Source (SLS) beamline X06SA at $\lambda = 1.0$ Å. One dataset diffracting to 1.8 Å was used for structure determination. The diffraction data was processed by the program XDS[44] in space group $P2_1$. Molecular replacement was performed with a polyA model of the SID from *Shewanella putrefaciens* (PDB ID: 2GPJ) using the program Phaser[45]. The model was then built in Coot[46] and refined with the software PHENIX[47] (Ramachandran favoured/outliers: 98.25%/0.22%).

Sybody generation against IrtAB

Sybodies were selected against C-terminally biotinylated *M. thermoresistibile* IrtAB as described previously[11]. These initial sybodies showed poor affinities, with the best binder displaying an affinity of only 238 nM. Furthermore, a large proportion of the sybodies were specific for the SID. To identify binders with higher affinity, a NestLink experiment was performed according to ref. [12] with the enriched pool of the second round of phage display using the loop and convex sybody libraries. According to the analysis of next generation sequencing (NGS), 578 unique loop sybodies were nested with 47,524 flycodes and 249 unique convex sybodies were nested with 17,628 flycodes. The nested libraries were expressed, purified by Ni^{2+}-NTA and monomeric pool members were isolated by SEC. Monomeric nested sybodies were then mixed with *M. thermoresistibile* IrtAB(ΔSID) and separated again by SEC (running buffer, 20 mM Tris-HCl pH7.4, 150 mM NaCl, 0.3% β-DM) to isolate sybody binders co-eluting with IrtAB(ΔSID). Flycodes were then isolated, analysed by liquid chromatography coupled with tandem mass spectrometry (LC–MS/MS) and ranked as described[12]. Genes of 11 loop sybodies and 5 convex sybodies were ordered (General Biosystems), expressed in the pBXNPHM3 vector (Addgene, 110099) and purified. Affinities of the purified sybodies were measured by SPR and were in the range of 74 nM–2.2 µM. Co-crystallization trails with *M. thermoresistibile* IrtAB(ΔSID) were performed with the two most affine sybodies and sybody Syb_NL5 ($K_D = 150$ nM) of the loop library yielded well-diffracting crystals.

Crystallization, data collection and structure determination of *M. thermoresistibile* IrtAB(ΔSID)

SEC-purified IrtAB(ΔSID) was concentrated to 7.9 mg ml^{-1} (63 µM). The sybody Syb_NL5 was added to a final concentration of 50 µM, thereby diluting IrtAB(ΔSID) to a final concentration of 47 µM. The protein was crystallized at 4 °C by sitting-drop vapour diffusion by mixing 2 µl protein and 2 µl mother liquor containing 28% (v/v) PEG400, 200 mM NaCl and 100 mM HEPES pH 7.5. Crystals appeared within three days, were cryo-protected using 30% PEG400 and frozen in liquid nitrogen. Crystals were measured at the Swiss Light Source (SLS) beamline X06DA at $\lambda = 1.0$ Å. One dataset diffracting to 2.7 Å was used for

structure determination. The diffraction data was processed by the program XDS[44] in space group $P2_1$. A polyalanine model of TM287 was manually fitted into the 7 Å cryo-EM density of IrtAB and used as the search model to solve the IrtAB structure by molecular replacement using the program Phaser[45]. A complete model for IrtAB(ΔSID) and Syb_NL5 was then built in Coot[46] and refined with BUSTER (https://www.globalphasing.com) and PHENIX[47] (Ramachandran favoured/outliers: 94.22%/0.47%).

Structural analyses

The X-ray structures of the SID and IrtAB(ΔSID) were fitted into the cryo-EM density map using Chimera[48] by placing them first manually close to the density and then using the Fit in Map tool. In case of IrtAB(ΔSID), the structures were fitted in both possible orientations regarding the homologous IrtA and IrtB chain and average map values of 0.01218 (correct orientation) and 0.01008 (wrong orientation) were obtained. For the SID, both possible positions were tried and resulted in average map values of 0.01207 (correct orientation) and 0.01039 (wrong orientation). Superimpositions of structures were performed using the MatchMaker tool of Chimera. The Nidelmann–Wunsch alignment algorithm and Blossom-62 matrix was used. r.m.s.d. ($Å^2$) values were calculated over the entire polypeptide chains—that is, without pruning of long atom pairs. Inward-facing cavities of IrtAB and TM287/288 (Fig. 1c) were calculated using the Channel Extract tool of the 3V web server[49] using a shell probe radius of 9 Å and a solvent-excluded probe radius of 3 Å. Figures were prepared using Chimera[48].

Redox measurements of SIDs

Redox experiments with the purified *M. thermoresistibile* and *M. smegmatis* SID proteins (wild-type and 3×E mutant) were performed under anaerobic conditions using a N_2-purged continuous-flow anaerobic chamber. All solutions were made oxygen-free on a Schlenk-line by four alternating cycles of vacuum and argon-flow. Proteins were diluted to final concentrations of 5 µM using TBS pH 7.5 and 10% glycerol. 100 µM ferene was added to the samples to monitor Fe(III) reduction via Fe(II)–ferene complex formation (λ_{max} = 590 nm)[16]. Fe(III)-cMBT or Fe(III)-MBT were added to a final concentration of 100 µM. Excess NADPH (final concentration 2 mM) was added to initiate ferric reduction. UV-Vis absorption spectra were recorded at 10-min intervals at 37 °C and ΔA_{590} at time t was obtained by subtracting the initial A_{590} at time = 0 min. As a control, the same reaction was performed with the *M. smegmatis* SID(3×E) mutant. Redox measurements were conducted with two biological replicates and representative data are shown. For Fe-MBT concentration-dependence experiments (Extended Data Fig. 7b), the measurements were performed in a 96-well-plate format as at least technical triplicates for every data point, sealed with a clear tape and the absorbance at 590 nm was measured using a Tecan Spark 20M at 37 °C. The generated Fe(II) was quantified using a Fe(II)–ferene calibration curve recorded at the same wavelength.

Biotinylation and SPR measurements of the SID of *M. smegmatis*

The *M. smegmatis* SID constructs (wild-type and 3×E mutant) were expressed in the pBXNH3A vector, which allows for N-terminal biotinylation via the Avi-tag[50]. Expression and purification were performed as described above. Biotinylation was performed simultaneously with 3C protease cleavage overnight. For biotinylation, 5 mM ATP, 10 mM MgOAc, 1.2-fold molar excess of biotin and 16 µg ml^{-1} BirA were added. The biotinylated SID constructs were used for SPR measurement using a Biacore T100 instrument (GE Healthcare). Approximately 15,000 response units of the SID constructs were coated onto a Sensor Chip CM5 (GE Healthcare). Afterwards, the coated lanes were saturated by coating with biotin-labelled BSA (Sigma) to avoid unspecific binding of cMBT to the surface of the chip. HPLC purified Fe-cMBT (molecular mass 799 Da) was used as the analyte at concentrations of 0, 6.25, 12.5, 25, 50 and 100 µM. Measurements were conducted as technical duplicates.

Production of ^{55}Fe-cMBT

^{55}Fe-cMBT was prepared according to ref. [5]. 200 µM Fe-cMBT in H_2O was mixed with 50 mM EDTA pH 4 in a 1:1 volume ratio. The solution was incubated overnight at room temperature while shaking. The solution was filtered with a 0.22-µm filter (Whatman) and desferrated cMBT was extracted with one volume of chloroform. The chloroform phase was washed twice with one volume of H_2O and evaporated. Desferrated cMBT was taken up in 100% ethanol and 0.4 mCi $^{55}FeCl_3$ (PerkinElmer) was added. Remaining desferrated cMBT was saturated by dropwise addition of cold $FeCl_3$ until no further increase in red colour was observed. ^{55}Fe-cMBT was purified again by extraction with one volume of chloroform and washed twice with one volume of H_2O to remove free $^{55}Fe^{3+}$ and Fe^{3+}.

^{55}Fe-cMBT uptake in *M. smegmatis* cells

M. smegmatis DKO and TKO cells, as well as *M. smegmatis* TKO cells complemented with different IrtAB constructs using the pFlag vector[24,51], were grown in 7H9 for 3 nights at 37 °C while shaking (140 rpm). 2 ml of these pre-cultures were used to inoculate 100 ml of MM supplemented with 6.88 µM $ZnSO_4$, 1.82 µM $MnSO_4$, 1.64 mM $MgSO_4$ and 0.5% (v/v) Tween 80 (treated with aluminium-oxide) in 1-l plastic roller bottles (Corning). Cells were grown for approximately 24 h until they reached an optical density at 600 nm (OD_{600}) of 3–5. The cultures were adjusted to an OD_{600} of 3 by diluting with medium. Six 1 ml aliquots of each strain or construct were placed on ice. 2 µl of ^{55}Fe-cMBT stock solution was added to reach final concentrations of 2 µM. Three aliquots (technical triplicates) were then incubated at 37 °C while the remaining three aliquots were kept on ice (for background subtraction). At each time point, 200 µl from each replicate were filtered using a 96-well vacuum manifold equipped with a glass fibre filter (Filtermat A, PerkinElmer). Filtration was immediately followed with two washing steps using 200 µl ice-cold medium. After all samples had been filtered and washed, the glass fibre filter was removed from the vacuum manifold and fused with a melt-on scintillator sheet (MeltiLex A scintillation gel, PerkinElmer) at 65 °C for 15 min. Radioactivity of incorporated hot iron was measured with MicroBeta Trilux Counter (PerkinElmer) by counting for 2 min in the 'Paralux Low-Background' mode. For each time point, the values obtained of the samples on ice were subtracted from the values obtained of samples incubated at 37 °C[5]. Experiments were conducted twice as biological replicates and representative data are shown.

Reconstitution of *M. thermoresistibile* IrtAB into proteoliposomes and ^{55}Fe-cMBT uptake

Purified *M. thermoresistibile* IrtAB (wild-type and 2×EQ mutant) was reconstituted into proteoliposomes as described previously[22]. In brief, 0.2 ml of purified protein at a concentration of 1 mg ml^{-1} was added to detergent-destabilized liposomes in 50 mM KP_i pH 7.0 with 20% (v/v) glycerol. Detergent was then removed by subsequent addition of fresh Bio-Beads (BioRad). Inclusion of an ATP-regenerating system (10 mM ATP, 10 mM $MgSO_4$, 24 mM Na_2-creatine phosphate and 2.4 mg ml^{-1} creatine kinase) was also performed according to ref. [22], and the proteoliposomes were kept in 100 mM KP_i pH 7.0 after the inclusion. Proteoliposomes at a final lipid concentration of 5 mg ml^{-1} were used for the ^{55}Fe-cMBT uptake experiments. ^{55}Fe-cMBT was added at a final concentration of 10 µM (corresponding to approximately 300,000 counts per min (cpm)) to the proteoliposomes, which were pre-incubated for 2 min at 37 °C, and the reaction was continued at 37 °C while shaking. At time intervals of 0.5, 2, 5 and 15 min, 3 aliquots of 40 µl (technical triplicates) were taken from the reaction. The samples were immediately centrifuged with ice-cold Micro Bio-Spin P-30 columns (BioRad, pre-equilibrated twice with 500 µl ice-cold 100 mM KPi pH 7.0 buffer) for 4 min at 1,000*g* at 4 °C to separate proteoliposomes from free ^{55}Fe-cMBT. The elution containing the proteoliposomes was mixed with 220 µl scintillation liquid. The samples were transferred to a

96-well Isoplate-96 (PerkinElmer) and measured with a MicroBeta Trilux Counter (Wallac) by counting for 2 min in the 'Paralux Low-Background' mode. The entire assay was performed twice with liposomes charged independently with the ATP regeneration system and representative data are shown.

Reconstitution of *M. thermoresistibile* IrtAB into nanodiscs and ATPase activity measurements

M. thermoresistibile IrtAB (wild-type and 2×EQ mutant) was concentrated after elution from the Ni^{2+}-NTA gravity flow column and gel-filtrated using Superose 6 Increase 10/300 GL (GE Healthcare) size-exclusion column in TBS containing 0.03% β-DDM. The non-cleaved proteins (still containing GFP fused to the C terminus of IrtB) were then reconstituted into nanodiscs. To this end, approximately 1 mg protein was mixed with MSP1D1E3 (prepared in house) and *E. coli* polar lipids in a molar ratio of 240:8:1 of lipids:MSP1D1E3:IrtAB, in a final volume of 200 µl. Lipids were prepared as follows: *E. coli* polar lipids in chloroform (Avanti) were mixed 3:1 (w/w) with L-α-phosphatidylcholine from egg yolk and evaporated. Dried lipids were dissolved in 20 mM HEPES pH 8.0, 0.5 mM K-EDTA, 100 mM NaCl and 100 mM cholate to a final concentration of 38 mg ml^{-1} and filtered using a 0.22-µm filter. The reconstitution mixture was incubated for 20 min at 25 °C while shaking. 600 mg (3 mg $µl^{-1}$ reconstitution mixture) Bio-Beads (BioRad) were added and the mixture was incubated at 4 °C while shaking for 6 h. Bio-Beads were removed by filtration and the sample containing reconstituted protein diluted 1:20 with TBS. 1.5 ml (3 ml slurry) HiTrap Ni^{2+}-NTA (Qiagen) was added and batch binding was performed for 30 min at 4 °C with end-over-end rotation. The resin was washed with 30 volumes of wash buffer (50 mM imidazole pH 7.5, 150 mM NaCl) and then incubated with 3C protease for 2 h at 4 °C with end-over-end rotation. The loaded resin was then transferred into an empty column to elute the cleaved protein reconstituted into nanodiscs. The sample was then gel-filtrated with a Superose 6 Increase 10/300 GL (GE Healthcare) size-exclusion column in TBS. Fractions corresponding to reconstituted IrtAB protein were collected and the concentration determined by the absorbance at 280 nm (A_{280}). ATPase activity was determined by incubation of 10 to 15 nM reconstituted proteins at 37 °C for 1 h with 2.5 mM ATP and a final concentration of 10 mM $MgSO_4$. A malachite green-molybdate solution was added as described previously to detect the release of inorganic phosphate by measuring the absorbance at 640 nm[52]. Substrates were added at final concentrations ranging from 0.5 to 40 µM to the protein before the incubation with ATP. All measurements were performed as technical triplicates, and the values of the IrtAB 2×EQ mutant were used for background subtraction. The ATPase assays with Fe-cMBT and Fe-MBT added at different concentrations (Fig. 2a) were conducted as three biological replicates and representative data are shown. ATPase assays with HPLC-purified mycobactins (Extended Data Fig. 6c, d) were performed as a single biological replicate.

Generation of gene deletions and complementation strains in *M. smegmatis*

Gene deletions in *M. smegmatis* were generated as previously described[24]. In brief, upstream and downstream flanking regions of the genes of interest were amplified from genomic DNA, cloned into pINIT and sequenced. The following primers (Supplementary Table 1) were used: #21/#22 and #23/#24 for *mbtD* (*msmeg_4512*); #25/#26 and #27/#28 for *fxbA* (*msmeg_0014*); #29/#30 and #31/#32 for *fxbBC* (*msmeg_0019*); #33/#34 and #35/#36 for *irtAB* (*msmeg_6553/6554*). Subsequently, the flanking regions were transferred into the pKO (apramycin) vector (Addgene, 110088) by FX cloning. Approximately 1 µg of pKO vector containing the flanking regions was transformed into electrocompetent *M. smegmatis* cells and plated on 7H10 plates with apramycin. Apramycin-resistant clones were tested for the first recombination event by PCR. PCR-positive clones were grown in the absence of apramycin to allow for a second recombination event, and then plated on 7H10 plates containing 20% sucrose and 0.2% 2-deoxy-galactose. Clones were screened for deletion of the gene of interest by colony PCR. Colony PCR-positive clones were confirmed by PCR from isolated genomic DNA. For complementation, *M. smegmatis* IrtAB constructs were cloned in the pFlag vector[24]. Approximately 250 to 500 ng of pFlag vector with the respective construct was co-transformed with pMA_int (Addgene, 110096) into electrocompetent *M. smegmatis* Δ*mbtD*Δ*fxbA*Δ*irtAB* cells and plated on 7H10 plates with apramycin[24]. Apramycin-resistant clones were confirmed by colony PCR for integration of the pFlag constructs.

Mycobactin-dependent growth assays in *M. smegmatis*

M. smegmatis strains with or without integrated pFlag constructs were grown in 7H9 to stationary phase (3 to 4 nights) by inoculation from glycerol stocks. These precultures were inoculated 1:100 in 1 ml minimal medium with or without 200 µM 2,2′-dipyridyl (added from a 1,000× stock in ethanol). The cultures were supplemented with 0.5% (v/v) Tween-80 to avoid cell clumping, and with different concentrations of Fe-cMBT and Fe-MBT crude extracts. 20% Tween-80 stock solutions were autoclaved with 2% (w/v) aluminium oxide and then filtered to remove traces of free iron. Antibiotics were not added for strains carrying pFlag constructs, as pFlag remains stably integrated into the genome even in the absence of antibiotic selection[24]. Cultures were grown for 5 days in plastic 96-deep-well plates (Treff Lab), with each strain grown in triplicates. 50 µl aliquots were taken every 24 h and transferred to a clear 96-well Microplate (Greiner) for OD_{600} determination. All growth assays shown were performed at least with three biological replicates on different days and representative data are shown.

Reporting summary

Further information on research design is available in the Nature Research Reporting Summary linked to this paper.

Data availability

The crystal structures of the SID and IrtAB-Syb_NL5 have been deposited in the Protein Data Bank (PDB) under entries 6TEK and 6TEJ, respectively The cryo-EM map has been deposited in the Electron Microscopy Data Bank under accession number EMD-10319. Plasmids, strains, the sybody Syb_NL5 and raw data are available from the authors upon reasonable request.

30. Ratledge, C. & Ewing, M. The occurrence of carboxymycobactin, the siderophore of pathogenic mycobacteria, as a second extracellular siderophore in *Mycobacterium smegmatis*. *Microbiology* **142**, 2207–2212 (1996).
31. Geertsma, E. R. & Dutzler, R. A versatile and efficient high-throughput cloning tool for structural biology. *Biochemistry* **50**, 3272–3278 (2011).
32. Mastronarde, D. N. Automated electron microscope tomography using robust prediction of specimen movements. *J. Struct. Biol.* **152**, 36–51 (2005).
33. Scheres, S. H. RELION: implementation of a Bayesian approach to cryo-EM structure determination. *J. Struct. Biol.* **180**, 519–530 (2012).
34. Zivanov, J. et al. New tools for automated high-resolution cryo-EM structure determination in RELION-3. *eLife* **7**, e42166 (2018).
35. Zheng, S. Q. et al. MotionCor2: anisotropic correction of beam-induced motion for improved cryo-electron microscopy. *Nat. Methods* **14**, 331–332 (2017).
36. Rohou, A. & Grigorieff, N. CTFFIND4: fast and accurate defocus estimation from electron micrographs. *J. Struct. Biol.* **192**, 216–221 (2015).
37. Moeller, A. et al. Distinct conformational spectrum of homologous multidrug ABC transporters. *Structure* **23**, 450–460 (2015).
38. Chen, S. et al. High-resolution noise substitution to measure overfitting and validate resolution in 3D structure determination by single particle electron cryomicroscopy. *Ultramicroscopy* **135**, 24–35 (2013).
39. Rosenthal, P. B. & Henderson, R. Optimal determination of particle orientation, absolute hand, and contrast loss in single-particle electron cryomicroscopy. *J. Mol. Biol.* **333**, 721–745 (2003).
40. Scheres, S. H. W. & Chen, S. Prevention of overfitting in cryo-EM structure determination. *Nat. Methods* **9**, 853–854 (2012).
41. Heymann, J. B. & Belnap, D. M. Bsoft: image processing and molecular modeling for electron microscopy. *J. Struct. Biol.* **157**, 3–18 (2007).
42. Cardone, G., Heymann, J. B. & Steven, A. C. One number does not fit all: mapping local variations in resolution in cryo-EM reconstructions. *J. Struct. Biol.* **184**, 226–236 (2013).

43. Tan, Y. Z. et al. Addressing preferred specimen orientation in single-particle cryo-EM through tilting. *Nat Methods* **14**, 793–796 (2017).
44. Kabsch, W. XDS. *Acta Crystallogr. D* **66**, 125–132 (2010).
45. McCoy, A. J. et al. Phaser crystallographic software. *J. Appl. Crystallogr*. **40**, 658–674 (2007).
46. Emsley, P. & Cowtan, K. Coot: model-building tools for molecular graphics. *Acta Crystallogr. D* **60**, 2126–2132 (2004).
47. Adams, P. D. et al. PHENIX: a comprehensive Python-based system for macromolecular structure solution. *Acta Crystallogr. D* **66**, 213–221 (2010).
48. Pettersen, E. F. et al. UCSF Chimera—a visualization system for exploratory research and analysis. *J. Comput. Chem*. **25**, 1605–1612 (2004).
49. Voss, N. R. & Gerstein, M. 3V: cavity, channel and cleft volume calculator and extractor. *Nucleic Acids Res*. **38**, W555–W562 (2010).
50. Bukowska, M. A. et al. A transporter motor taken apart: flexibility in the nucleotide binding domains of a heterodimeric ABC exporter. *Biochemistry* **54**, 3086–3099 (2015).
51. Hohl, M. et al. Increased drug permeability of a stiffened mycobacterial outer membrane in cells lacking MFS transporter Rv1410 and lipoprotein LprG. *Mol. Microbiol*. **111**, 1263–1282 (2019).
52. Hohl, M. et al. Structural basis for allosteric cross-talk between the asymmetric nucleotide binding sites of a heterodimeric ABC exporter. *Proc. Natl Acad. Sci. USA* **111**, 11025–11030 (2014).

Acknowledgements We thank all members of the Seeger laboratory for discussions; B. Blattmann, C. Stutz-Ducommun and S. Eberle of the Protein Crystallization Center UZH for performing the crystallization screening; the staff of the SLS beamlines X06SA and X06DA for their support during data collection; and J. Sobeck of the Functional Genomics Center Zurich for support during SPR measurements. We also thank all members of the Medalia laboratory, especially M. Eibauer, for discussions and the Center for microscopy and image analysis (ZMB) of the UZH for providing help and equipment. Work in the laboratory of M.A.S. was supported by the European Research Council (ERC) (consolidator grant no. 772190), a SNSF Professorship of the Swiss National Science Foundation (PP00P3_144823) and a grant of the Novartis Foundation for Medical-Biological Research. Work in the laboratory of O.M. was supported by the Swiss National Science Foundation (grant 31003A_179418) and the Mäxi Foundation. Work in the laboratory of G.M. was supported by the Robert A. Welch Foundation (grant no. AT-1935-20170325) and by the National Institute of General Medical Sciences of the National Institutes of Health (R35GM128704). F.M.A., M.S.W. and I.G. were supported by three Candoc fellowships of the University of Zurich.

Author contributions F.M.A. and M.A.S. conceived the project. F.M.A. cloned all ORFs, established the protein purification protocols, and generated gene deletions in *M. smegmatis*. F.M.A. established the mycobactin extraction protocols with the help of S.A. and carried out the majority of the biochemical and in vivo characterization of IrtAB. F.M.A., I.G. and L.M.H. carried out ^{55}Fe-cMBT transport assays with intact cells and proteoliposomes. F.M.A. selected Syb_NL5 with the help of P.E. and I.Z. M.S.W. carried out all cryo-EM work and data analysis under the supervision of O.M. with samples prepared by F.M.A. F.M.A. solved the structure of the SID with the support of C.A.J.H. I.G. crystallized the IrtAB-Syb_NL5 complex with the help of F.M.A. and solved its structure with the help of M.A.S. I.G. built the IrtAB model with the support of C.A.J.H. and M.A.S. M.J.G. carried out the mycobactin reduction experiments under the supervision of G.M. E.E.P. purified mycobactins by HPLC under the supervision of J.P. F.M.A., M.S.W., I.G., G.M., O.M. and M.A.S. interpreted the data. F.M.A., M.S.W., I.G. and M.A.S. prepared figures, F.M.A., M.S.W. and M.A.S. wrote the paper, and I.G., G.M. and O.M. edited the paper.

Competing interests The authors declare no competing interests.

Additional information

Supplementary information is available for this paper at https://doi.org/10.1038/s41586-020-2136-9.

Correspondence and requests for materials should be addressed to M.A.S.

Peer review information *Nature* thanks Gregory Cook, Damian Ekiert, Georgia Isom and Jochen Zimmer for their contribution to the peer review of this work.

a

IrtAB sequence identity (%)			
	Mth	*Msm*	*Mtb*
Mth		73	71
Msm	73		71
Mtb	71	71	

b

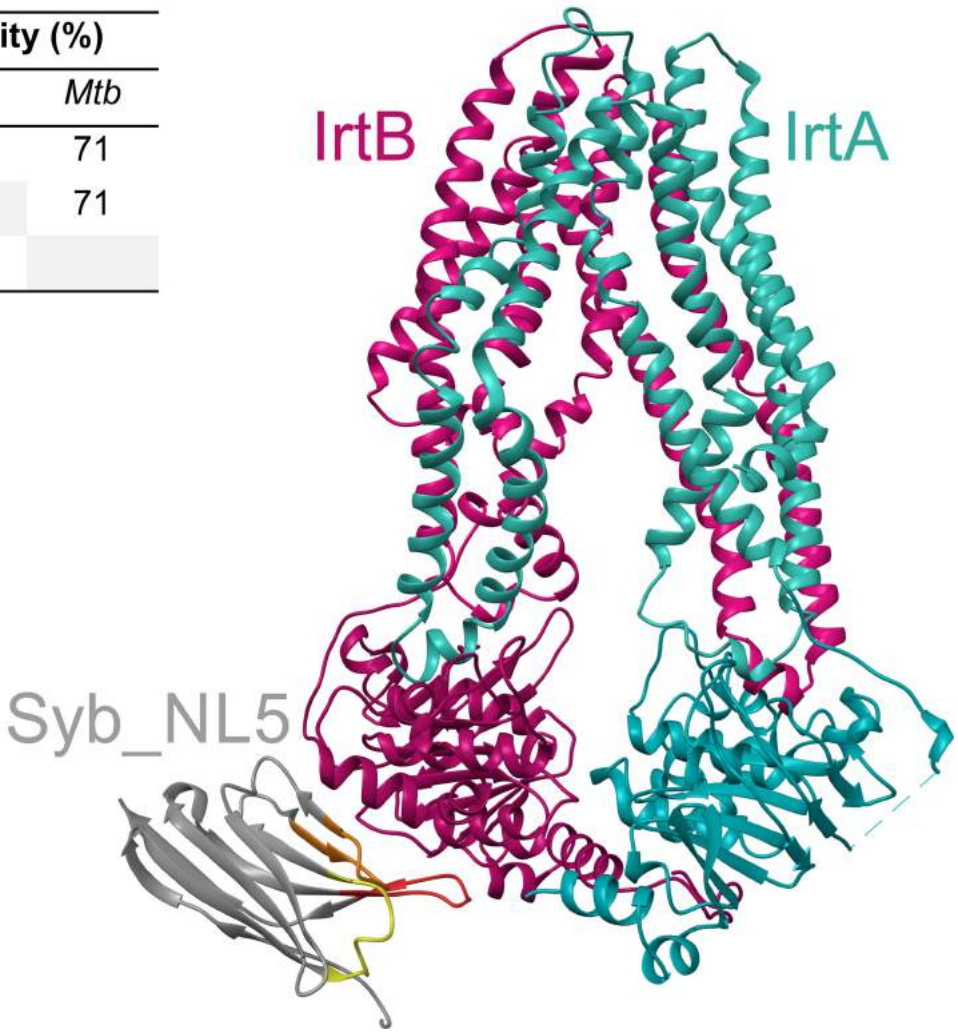

Extended Data Fig. 1 | Sequence identity of IrtAB homologues and crystal structure of IrtAB determined with the aid of a sybody. a, Sequence identity matrix of full-length IrtAB from *M. thermoresistibile* (*Mth*), *M. smegmatis* (*Msm*) and *M. tuberculosis* (*Mtb*). **b**, IrtAB(ΔSID) of *M. thermoresistibile* (lacking the SID and the linker between the SID and the TMD of IrtA) was crystallized with the aid of a sybody. IrtA is coloured in turquoise, IrtB in purple and the sybody in grey with CDR1, CDR2 and CDR3 coloured in yellow, orange and red, respectively. CDR, complementary determining region.

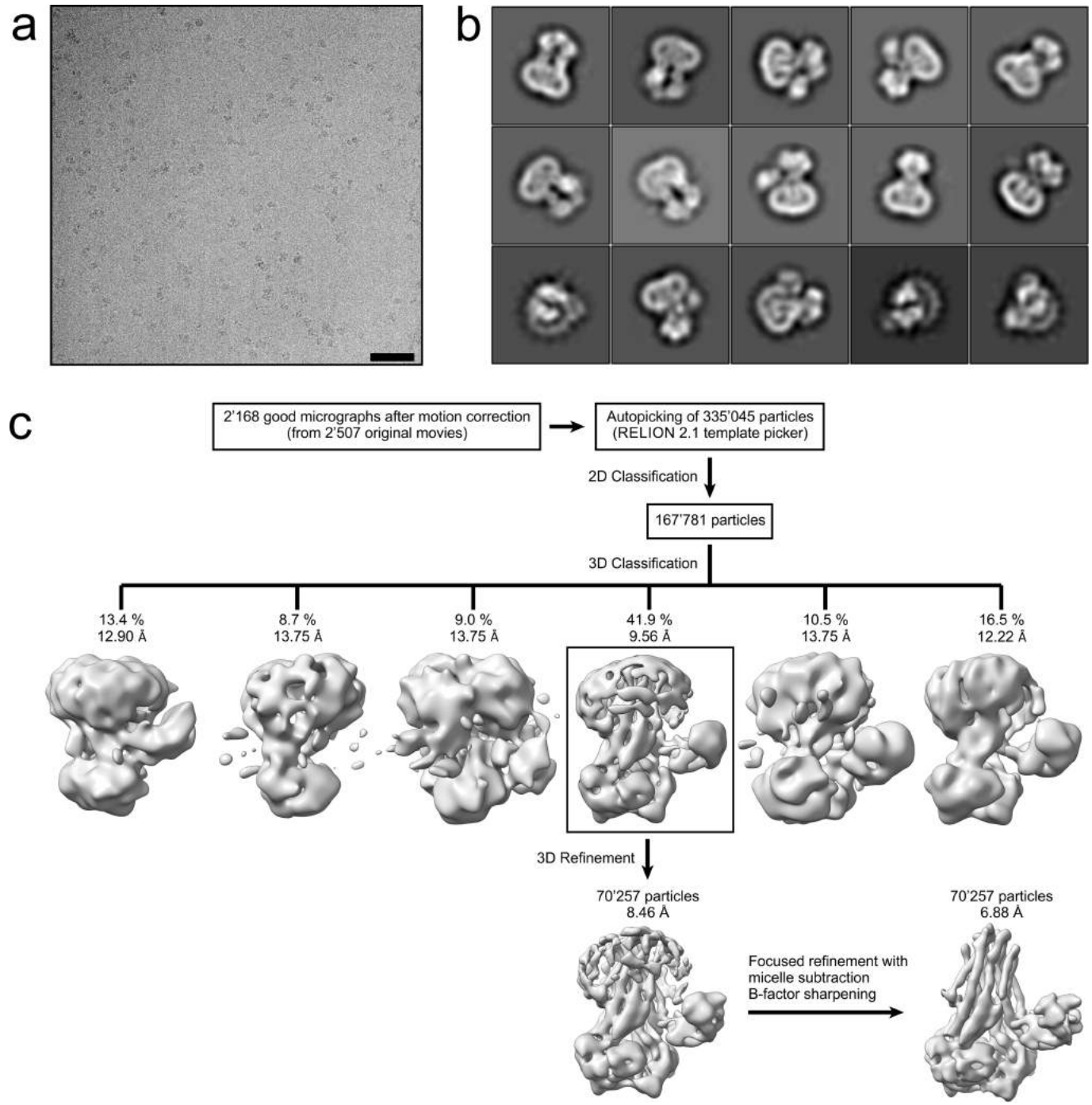

Extended Data Fig. 2 | Cryo-EM data processing of IrtAB. a, Typical motion-corrected cryo-EM micrograph of the detergent-solubilized IrtAB sample. Scale bar, 50 nm. **b**, Representative 2D class averages used for 3D reconstruction, showing side and bottom views. **c**, The data-processing workflow. High-quality micrographs (2,168) were selected after motion correction and used for autopicking of 335,045 particles. Several rounds of 2D classification were performed to remove false positives, yielding 167,781 IrtAB particles, which were subjected to 3D classification. One out of six classes (indicated by the black box), containing 70,257 particles, revealed distinct structural features of IrtAB with its SID and was subjected to 3D refinement. The resulting structure was used to subtract the detergent micelle from the raw particles. Afterwards, a focused 3D refinement without the detergent micelle was performed. The resulting map was sharpened using a B-factor of −319 $Å^2$. The final structure was resolved to 6.88 Å and reveals details of the TMDs, the NBDs and the SID.

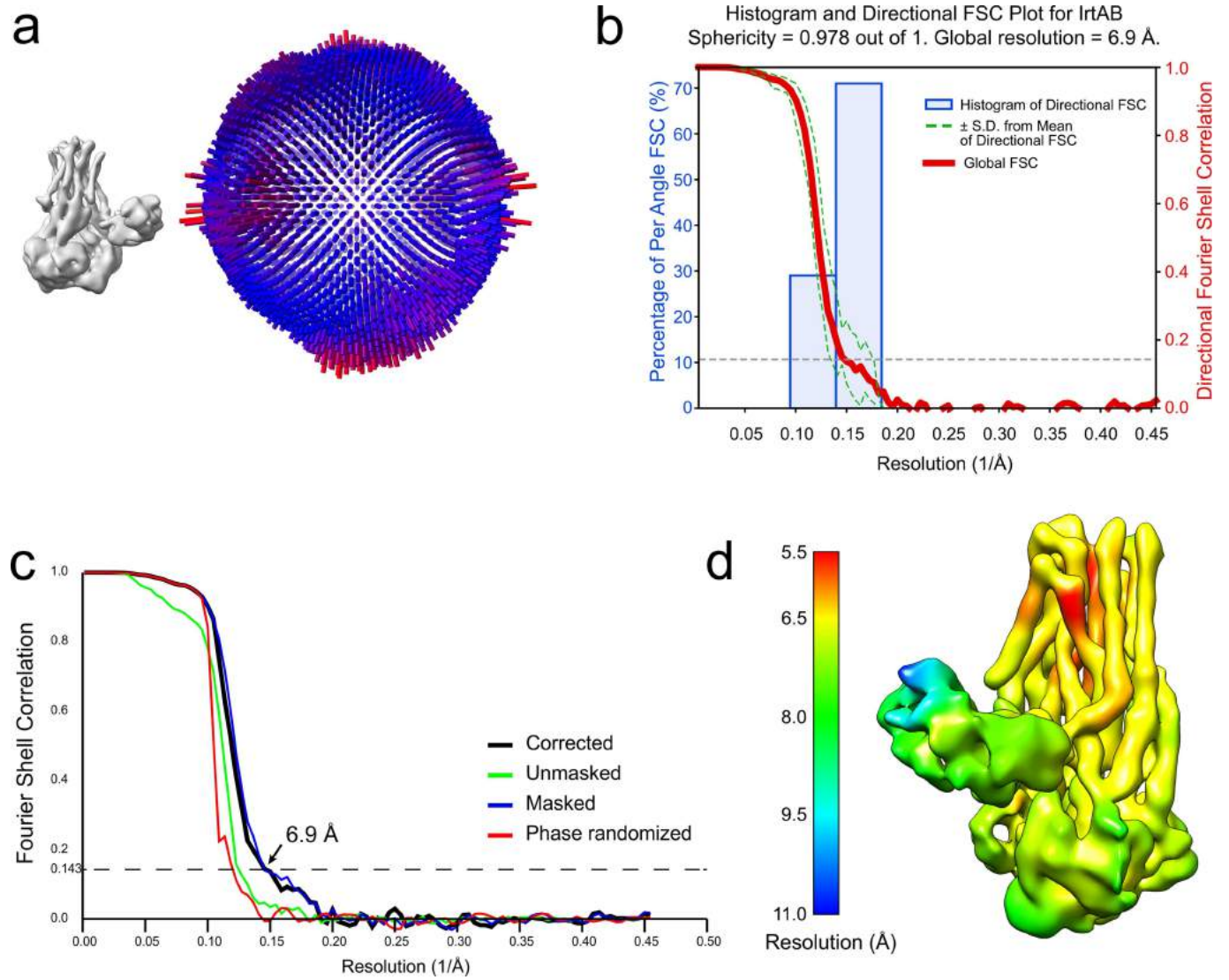

Extended Data Fig. 3 | Cryo-EM data validation. a, Angular distribution plot of all IrtAB particles that contributed to the final map. The map and the angular distribution plot have the same orientation. The height and colour (from blue to red) of the cylinder bars is proportional to the number of particles in those views. **b**, Plot of the directional FSC that represents a measure of directional resolution anisotropy. Shown are the global FSC (red line), the spread of directional resolution values defined by ±1 standard deviation from the mean of the directional resolutions (area encompassed by the green dotted lines) and a histogram of 100 directional resolutions evenly sampled over the 3D FSC (blue bars). A sphericity of 0.978 was determined at an FSC threshold of 0.5, which indicates very isotropic angular distribution (a value of 1 stands for completely isotropic angular distribution). The global resolution was determined to 6.9 Å (0.143 threshold). Directional FSC determination was performed with the 3DFSC software. **c**, FSC plot of the final density map of IrtAB. The plot shows the unmasked (green), masked (blue), phase randomized (red) and masking-effect-corrected (black) FSC curves. The resolution at which the gold-standard FSC curve drops below the 0.143 threshold is indicated. **d**, Local resolution variations in the cryo-EM map. The resolution ranges from 5.5 to 10.8 Å, as calculated by BlocRes.

a

Name	PDB ID	IrtA	IrtB
IrtA	6TEJ	-	5.872
IrtB	6TEJ	5.872	-
TM287 IF	4Q4H	4.312	5.849
TM288 IF	4Q4H	4.865	5.832
TmrA IF	5MKK	5.747	6.706
ABCB10 A IF	3ZDQ	5.836	6.009
TmrB IF	5MKK	5.955	6.864
NaAtm1 A IF	4MRN	6.695	6.901
CmABCB1 IF	3WMG	6.992	8.974
McjD A OCC	4PL0	7.774	6.959
TM287 OF	6QUZ	7.379	7.761
TmrB B OF	6RAH	7.404	7.542
TM288 OF	6QUZ	7.482	7.493
Sav1866 A OF	2HYD	7.619	8.559
TmrA OF	6RAH	7.853	8.261
MsbA OF	3B60	8.085	8.240
ABCD4 OF	6JBJ	8.783	12.235

b

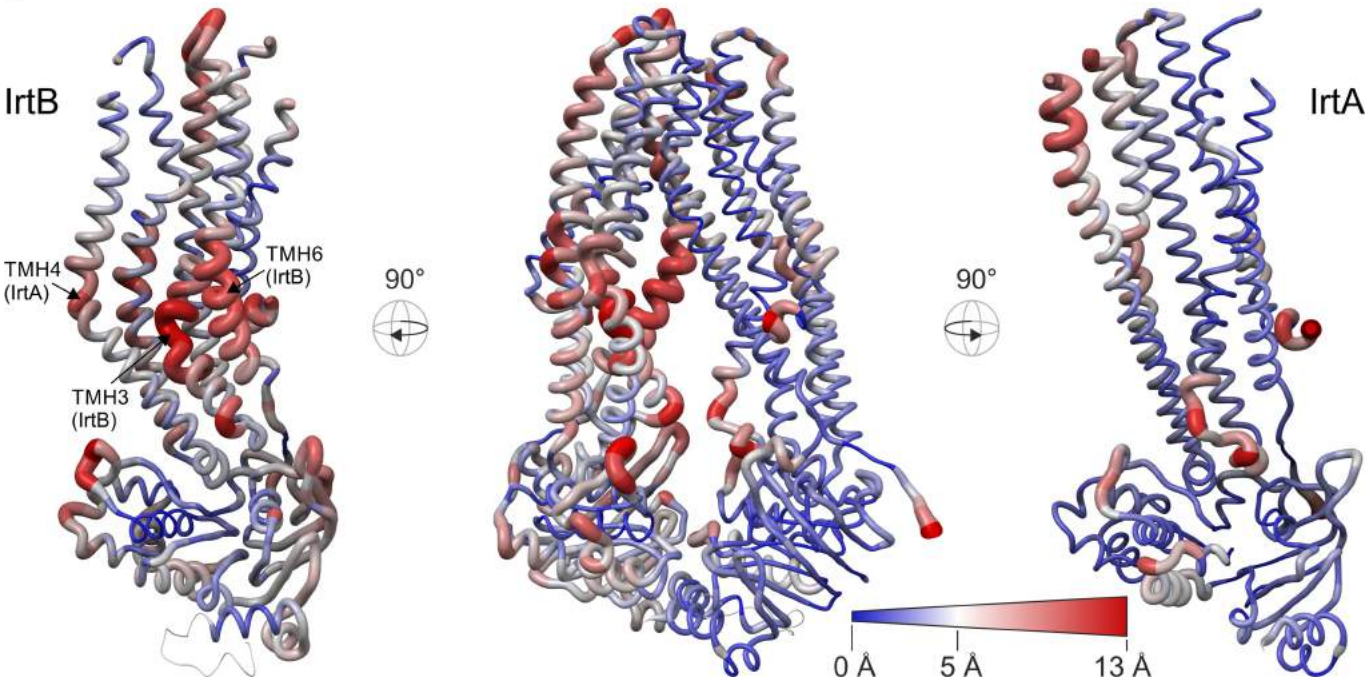

Extended Data Fig. 4 | Superimpositions with ABC exporter structures and structural comparison of IrtAB and TM287/288. a, Superimposition of ABC exporters using the MatchMaker tool of Chimera. Nidelmann–Wunsch alignment algorithm and Blossom-62 matrix was used. r.m.s.d. (Å^2) values were calculated over the entire polypeptide chains—that is, without pruning of long atom pairs. In the case that the asymmetric unit contained several polypeptides of identical sequence, chain A was taken for analysis (indicated as 'A' in the protein name). IF, inward-facing; OCC, occluded; OF, outward-facing. **b**, Structural deviations between IrtAB and the ABC exporter TM287/288 (PDB: 4Q4H). Shown is the structure of IrtAB in an 'open-book representation' with the entire transporter in the middle and the two half-transporters on the left (IrtB with domain-swap-helices TMH4 and TMH5 of IrtA) and on the right (IrtA with domain-swap-helices of IrtB). The structures are shown in sausage representation in which the thickness and colour gradient from blue to red indicate variable degrees of structural deviations between IrtAB and TM287/288. Major structural deviations in the TMDs of IrtB are indicated.

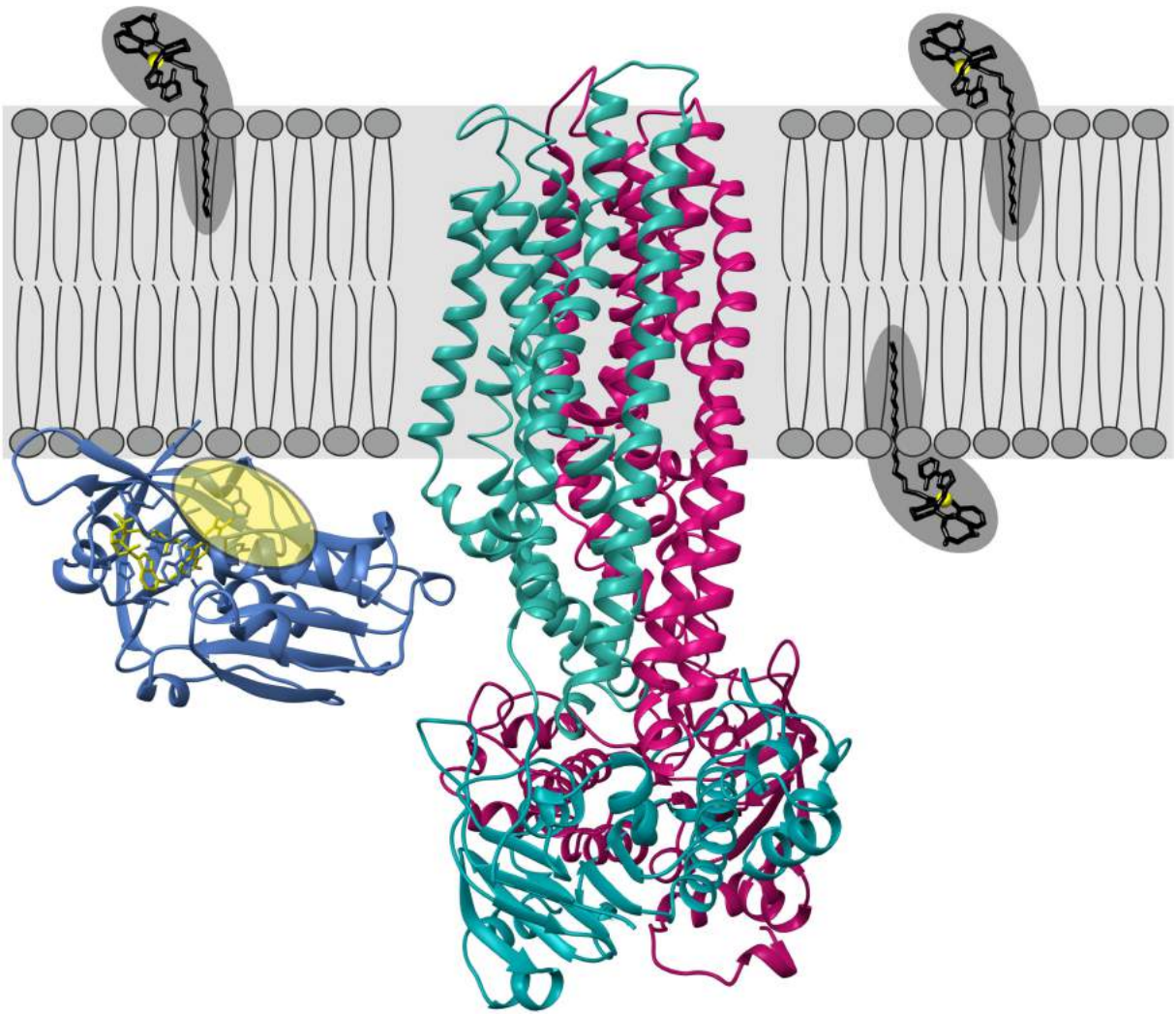

Extended Data Fig. 5 | Full-length IrtAB structure shown in the membrane context. MBT molecules with a C17 aliphatic chain length are shown in stick representation. The SID is orientated towards the membrane with its mycobactin binding pocket (yellow ellipsoid) facing the inner leaflet. IrtAB is coloured as in Fig. 1.

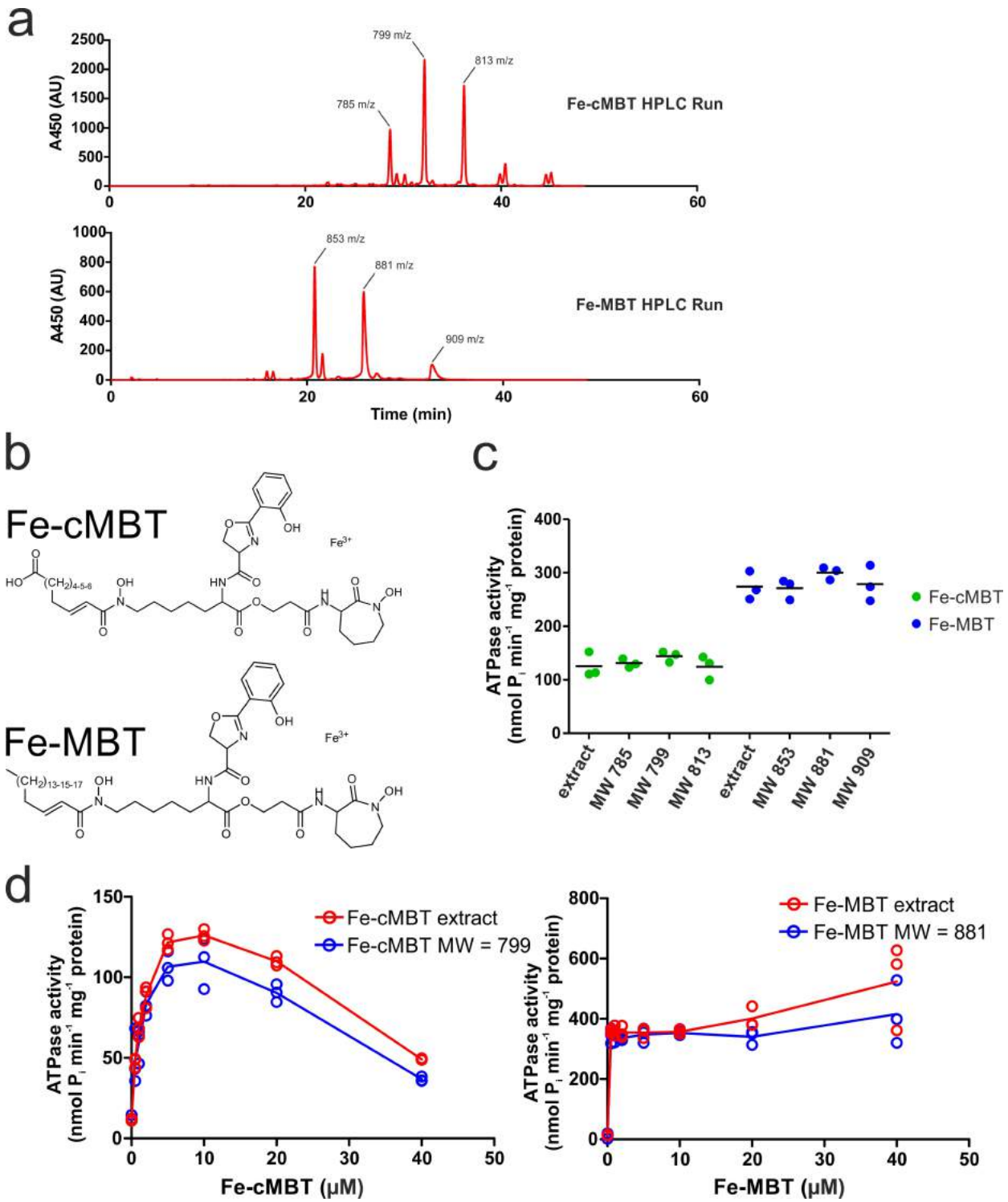

Extended Data Fig. 6 | ATPase activity measurements using HPLC-purified mycobactins of defined masses. a, Reversed-phase chromatography separation by HPLC of Fe-cMBT (top) and Fe-MBT (bottom) isolated from *M. smegmatis*. Masses of mycobactins giving rise to the main peaks were determined by mass spectrometry. These analyses were performed once. **b**, Chemical structures of Fe-cMBT and Fe-MBT. **c**, ATPase activities of nanodisc-reconstituted IrtAB measured in the presence of Fe-cMBT or Fe-MBT of defined mass isolated by HPLC. Crude extracts of mycobactins were included as controls. Mycobactins were added at a concentration of 5 μM. Data points are technical triplicates, which were used to calculate the mean value (black bar). **d**, ATPase stimulation curves determined over a range of mycobactin concentrations for HPLC-purified samples of defined mass or the respective crude extracts. Data points are technical triplicates and curves cross through the mean values.

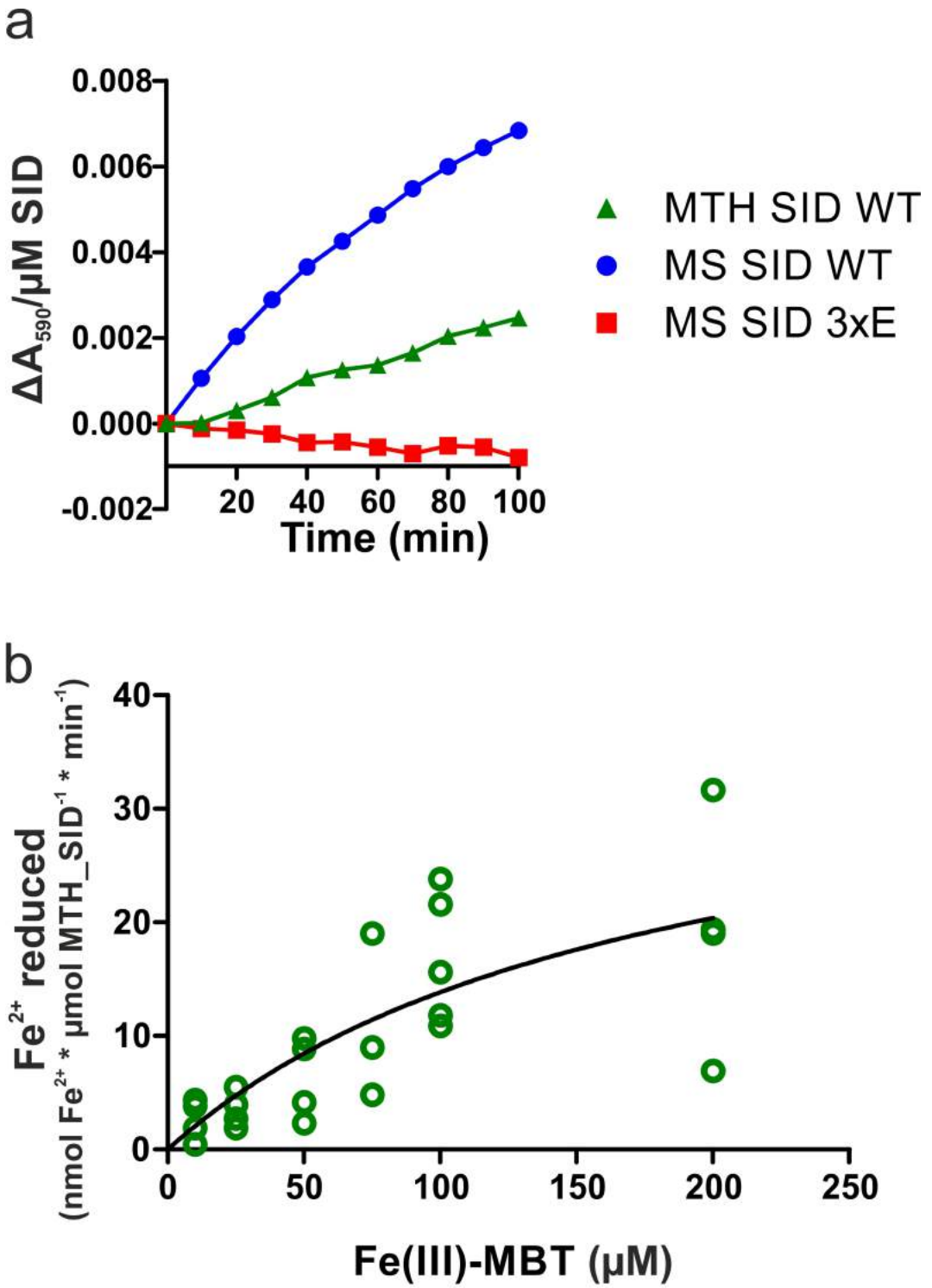

Extended Data Fig. 7 | Mycobactin reduction by purified SID. a, Reduction of Fe(III)-MBT (100 μM) by *M. thermoresistibile* and *M. smegmatis* SIDs using NADPH as an electron donor and ferene as a reporter probe of released Fe(II) (A_{max} = 590 nm). The 3×E mutant SID(3×E) served as a negative control. Representative data of biological duplicates are shown. **b**, Reduction of Fe(III)-MBT by the SID of *M. thermoresistibile* performed at different concentrations of Fe(III)-MBT. The data were fitted using the Michaelis–Menten equation. Data points are technical replicates.

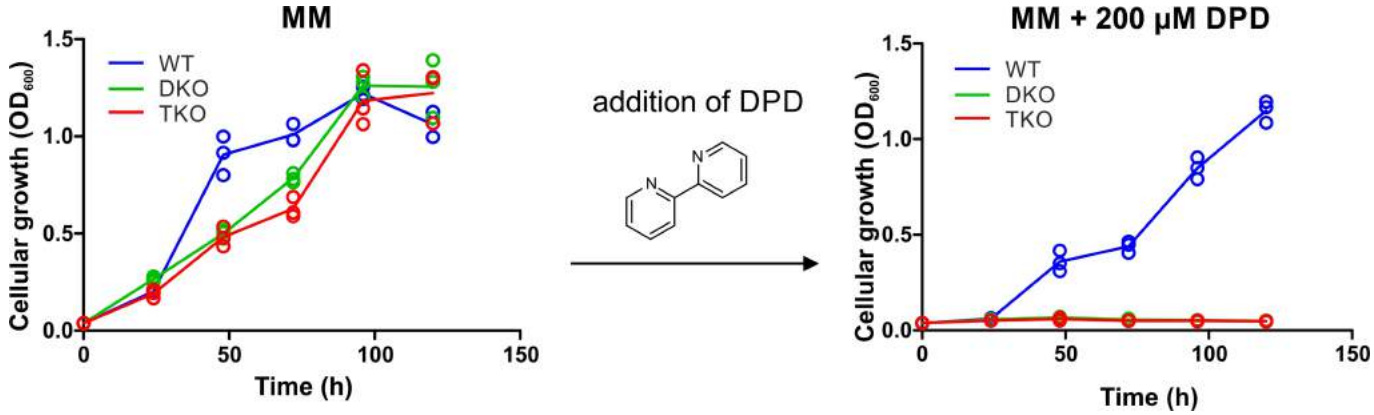

Extended Data Fig. 8 | Siderophore-dependent growth assay. When grown in minimal medium (MM) under controlled iron concentrations, wild-type *M. smegmatis*, the *M. smegmatis* Δ*fxbA*Δ*mbtD* double mutant (DKO) and the *M. smegmatis* Δ*fxbA*Δ*mbtD*Δ*irtAB* triple mutant (TKO) showed no significant differences in growth. Upon addition of the weak iron chelator 2,2′-dipyridyl, only the wild-type strain was able to grow owing to its ability to synthesize siderophores that extract iron bound to 2,2′-dipyridyl. Data points are technical triplicates and curves cross through the mean values.

Extended Data Table 1 | Cryo-EM data collection and processing statistics

	IrtAB full-length (EMD -10319)
Data collection and processing	
Magnification	45455
Voltage (kV)	300
Electron exposure (e–/Å^2)	85
Defocus range (μm)	-1.6 to -3.0
Pixel size (Å)	0.55 (in super-resolution) 1.10 (for reconstruction)
Symmetry imposed	C1
Initial particle images (no.)	335045
Final particle images (no.)	70257
Map resolution (Å)	6.88
FSC threshold	0.143
Map resolution range (Å)	5.5 to 10.8

Extended Data Table 2 | X-ray data collection and refinement statistics

	SID *	IrtAB apo, inward-facing †
Data collection		
Space group	$P2_1$	$P2_1$
Cell dimensions		
a, *b*, *c* (Å)	52.07, 111.7, 52.20	103.06, 78.58, 133.57
α, β, γ (°)	90.000, 119.755, 90.000	90.000, 98.204, 90.000
Resolution (Å)	1.8 (1.864 - 1.8) ‡	2.7 (2.797 - 2.700)
R_{sym} or R_{merge}	11.06 (68.53)	11.4 (182.5)
$I / \sigma I$	11.44 (2.94)	15.03 (1.21)
Completeness (%)	95.20 (97.36)	99.85 (99.69)
Redundancy	6.2 (6.0)	6.8 (6.9)
Refinement		
Resolution (Å)	45.32 - 1.80	47.43 – 2.70
No. reflections	45567 (4678)	58375 (5791)
R_{work} / R_{free}	0.2229 / 0.2546	0.2565 / 0.2907
No. atoms		
Protein	3674	9674
Ligand/ion	106	34
Water	520	54
B-factors		
Protein	23.39	92.27
Ligand/ion	15.10	107.25
Water	29.60	57.20
R.m.s. deviations		
Bond lengths (Å)	0.002	0.004
Bond angles (°)	0.53	0.99

*A single crystal was used for the SID structure.
†A single crystal was used for the IrtAB apo, inward-facing structure.
‡Values in parenthesis are shown for the highest-resolution shell.

nature research

Corresponding author(s): Markus A. Seeger

Last updated by author(s): Mar 14, 2020

Reporting Summary

Nature Research wishes to improve the reproducibility of the work that we publish. This form provides structure for consistency and transparency in reporting. For further information on Nature Research policies, see Authors & Referees and the Editorial Policy Checklist.

Statistics

For all statistical analyses, confirm that the following items are present in the figure legend, table legend, main text, or Methods section.

n/a	Confirmed
☐	☒ The exact sample size (*n*) for each experimental group/condition, given as a discrete number and unit of measurement
☐	☒ A statement on whether measurements were taken from distinct samples or whether the same sample was measured repeatedly
☒	☐ The statistical test(s) used AND whether they are one- or two-sided *Only common tests should be described solely by name; describe more complex techniques in the Methods section.*
☒	☐ A description of all covariates tested
☒	☐ A description of any assumptions or corrections, such as tests of normality and adjustment for multiple comparisons
☐	☒ A full description of the statistical parameters including central tendency (e.g. means) or other basic estimates (e.g. regression coefficient) AND variation (e.g. standard deviation) or associated estimates of uncertainty (e.g. confidence intervals)
☒	☐ For null hypothesis testing, the test statistic (e.g. *F*, *t*, *r*) with confidence intervals, effect sizes, degrees of freedom and *P* value noted *Give P values as exact values whenever suitable.*
☒	☐ For Bayesian analysis, information on the choice of priors and Markov chain Monte Carlo settings
☒	☐ For hierarchical and complex designs, identification of the appropriate level for tests and full reporting of outcomes
☒	☐ Estimates of effect sizes (e.g. Cohen's *d*, Pearson's *r*), indicating how they were calculated

Our web collection on statistics for biologists contains articles on many of the points above.

Software and code

Policy information about availability of computer code

Data collection	SerialEM 3.5.8, MCS version 2.5.0.5 as control software of Illumina MiSeq, Illumina RTA version 1.18.54 for base calling, bcl2fastq version 2.18.0.12 for demultiplexing of MiSeq
Data analysis	Excel, GraphPad Prism 5.04, SB Grid (XDS, Phenix, ccp4, Buster), RELION 2.1, RELION 3.0, MotionCor2, CTFFIND4, Bsoft package, 3DFSC

For manuscripts utilizing custom algorithms or software that are central to the research but not yet described in published literature, software must be made available to editors/reviewers. We strongly encourage code deposition in a community repository (e.g. GitHub). See the Nature Research guidelines for submitting code & software for further information.

Data

Policy information about availability of data

All manuscripts must include a data availability statement. This statement should provide the following information, where applicable:

- Accession codes, unique identifiers, or web links for publicly available datasets
- A list of figures that have associated raw data
- A description of any restrictions on data availability

The structures have been deposited in the PDB under accession numbers 6TEJ (M. thermoresistibile IrtAB_TRANS/Syb_NL5 complex) and 6TEK (M. thermoresistibile SID). The cryo-EM map has been deposited in the Electron Microscopy Data Bank under accession number EMD-10319.
Sybody Syb_NL5 will be made available upon reasonable request to the corresponding author.

Field-specific reporting

Please select the one below that is the best fit for your research. If you are not sure, read the appropriate sections before making your selection.

☒ Life sciences ☐ Behavioural & social sciences ☐ Ecological, evolutionary & environmental sciences

For a reference copy of the document with all sections, see nature.com/documents/nr-reporting-summary-flat.pdf

Life sciences study design

All studies must disclose on these points even when the disclosure is negative.

Sample size	Sample size estimation was not relevant for this study, as it does not report on a statistical evaluation of effects between two or more groups.
Data exclusions	No data were excluded from the analysis.
Replication	ATPase activity measurements were carried out with three technical replicates for each data point and these data were used to calculate mean values (Fig. 2a; Extended Data Figure 8c and d). The ATPase activity measurements shown in Fig. 2a were conducted as three biological replicates with different batches of purified and reconstituted IrtAB and different batches of isolated Fe-cMBT and Fe-MBT. All attempts at replication were successful. Representative data are shown. The ATPase activity measurements shown in Extended Data Figure 8c and d were conducted as a single biological replicate. In vitro 55Fe-cMBT transport experiments in proteoliposomes (Fig. 2b) were carried out twice on different days with vesicles charged independently with the ATP regeneration system. These attempts at replication were successful and representative data are shown. Each data point of proteoliposomes containing either wildtype or 2xEQ IrtAB was measured as technical triplicates to calculate mean values (Fig. 2b).The empty liposome and the buffer only control was measured as single values for each data point. In vivo 55Fe-cMBT transport assays (Fig. 3d and f) were conducted as biological duplicates (independently grown cell cultures on different days) in which every data point was measured as technical triplicates to calculate mean values (Fig. 3d and f). All attempts at replication were successful. Representative data of one biological replicate are shown. Cellular growth experiments were carried out at least with three biological replicates on different days and with technical triplicates for every data point. All attempts at replication were successful. Representative data are shown. Technical triplicate values were used to calculate mean values (Fig. 3 and Extended Data Figure 10). SPR assays were performed with one biological replicate and two technical replicates for each data point (Fig. 2e). Fe(III)-cMBT reduction data (Fig. 2d and Extended Data Figure 9a) were measured twice as as biological replicates using two batches of purified SID proteins. Attempts of replication were successful. Representative data (without error bars) are shown. For the determination of the apparent KM of Fe-MBT (Extended Data Fig. 9b), the assay was performed once with three technical triplicates for every data point to calculate mean values through which the data were fitted using a hyperbolic equation.
Randomization	Animals or human research participants were not involved in this study and, as such, samples were not randomized for the experiments.
Blinding	Animals or human research participants were not involved in this study and, as such, samples were not blinded for the experiments.

Reporting for specific materials, systems and methods

We require information from authors about some types of materials, experimental systems and methods used in many studies. Here, indicate whether each material, system or method listed is relevant to your study. If you are not sure if a list item applies to your research, read the appropriate section before selecting a response.

Materials & experimental systems

n/a	Involved in the study
☐	☒ Antibodies
☒	☐ Eukaryotic cell lines
☒	☐ Palaeontology
☒	☐ Animals and other organisms
☒	☐ Human research participants
☒	☐ Clinical data

Methods

n/a	Involved in the study
☒	☐ ChIP-seq
☒	☐ Flow cytometry
☒	☐ MRI-based neuroimaging

Antibodies

Antibodies used	The synthetic nanobody (sybody) Syb_NL5, which was generated as part of this study.

Validation	The affinity was determined by SPR (150 nM) and its structure was solved in complex with IrtABΔSID (M. thermoresistibile homologue) by X-ray crystallography. The sybody was not validated for Western blotting or immunohistochemistry.